Oxidation extent of the upper mantle by subducted slab and possible oxygen budget in deep Earth inferred from redox kinetics of olivine

Chengcheng Zhao[1], Takashi Yoshino[1], and Baohua Zhang[2]

[1]Institute for Planetary Materials
[2]Zhejiang University

November 24, 2022

Abstract

Redox input by subducting slab into deep mantle is of vital importance for deep cycle and isotopic evolution of volatile elements, whose chemically stable forms are controlled by redox state. Lithospheric mantle is crucial in redefining redox state of the Earth's deep mantle. To constrain to which extent subducted slab can modify redox state of the upper mantle and how much oxygen slab can carry into deep Earth, we investigated redox kinetics of olivine adopting diffusion couple methods at 1 GPa and 1373-1573 K in a piston cylinder apparatus. It is found that redox process in olivine is diffusion-controlled, and diffusing on the order of 10-12 m2/s at 1473 K. The oxidation process in initially reduced olivine is oxygen fugacity (fO2)-independent with activation enthalpy of 235 ± 56 kJ/mol, while the reduction process in initially oxidized olivine is fO2-dependent with an exponent of 2/5. Diffusion profile analysis reveals that redox state of starting material plays decisive role in determining redox mechanism. Below ΔFMQ+1, redox process in olivine is controlled by oxygen grain boundary diffusion, while above ΔFMQ+1, it is rate-limited by faster diffusion species which might be hydrogen related Mg vacancy. The extremely slow redox rate limits the homogenization of the slab and its surrounding mantle as redox state of the upper mantle remains unchanged for over past 3.5 Gyrs. The subducted slab has the ability to efficiently transport oxidized components to the region deeper than the mantle transition zone. A highly underestimated oxygen reservoir may have formed in the deep Earth.

Hosted file

Table S1 Experimental summary for sintering Pt-doped olivine aggregate using piston-cylinder apparatus

Run No.	Starting material	Capsule	T (K)	Duration (mins)	log fO$_2$	log fO$_2$ (ΔIW)	Grain size (μm)
PC699	Ol+3wt%SiO$_2$+5wt%Pt (oxidized)	Ni foil	1473	30	-4.3(0.3)	7.3(0.3)	3.3(1.7)
PC665					-4.5(0.4)	7.1(0.3)	3.1(1.7)
PC687					-1.9(0.3)	9.7(0.3)	/
PC686	Ol+3wt%SiO$_2$+5wt%Pt (reduced)	Mo foil	1473	30	-10.4(0.3)	1.1(0.3)	2.3(1.2)
PC674				15	-10.4(0.2)	1.2(0.2)	2.7(1.2)
PC714	Ol+3wt%SiO$_2$+5wt%Pt (reduced/oxidized)	Ni foil	1473	30	-3.9(0.6)	7.6(0.6)	2.5(1.2)
		Mo foil			-10.3(0.1)	1.2(0.1)	2.3(1.4)
PC710	Ol+3wt%SiO$_2$+5wt%Pt (reduced/oxidized)	Ni foil	1373	30	-6.7(0.3)	6.2(0.3)	2.3(1.1)
		Mo foil			-11.5(0.4)	1.3(0.4)	2.3(1.1)
PC718	Ol+3wt%SiO$_2$+5wt%Pt (reduced/oxidized)	Ni foil	1573	30	-6.0(0.4)	4.4(0.4)	2.0(1.1)
		Mo foil			-8.9(0.2)	1.6(0.2)	3.7(2.3)

Log fO$_2$ (ΔIW) demonstrates oxygen fugacity difference between sample and iron-wustite (IW) buffer under certain P, T condition. Number in parenthesis is the calculated standard deviation of corresponding data. "/" in run PC687 means that its grain size is not measured.

2

Oxidation extent of the upper mantle by subducted slab and possible oxygen budget in deep Earth inferred from redox kinetics of olivine

Chengcheng Zhao [1] * †, Takashi Yoshino[1], Baohua Zhang[2]

[1] Institute for Planetary Materials, Okayama University, Misasa, Tottori 682-0193, Japan.

[2] Key Laboratory of Geoscience Big Data and Deep Resource of Zhejiang Province,

Institute of Geology and Geophysics, School of Earth Sciences, Zhejiang University,

Hangzhou 310027, China.

* Corresponding author. E-mail: cczhao_zhao@outlook.com

† Current address: Laboratoire Magmas et Volcans CNRS, IRD, OPGC, Université

Clermont Auvergne, 63000 Clermont-Ferrand, France

Key points:

- Redox kinetics of olivine was investigated by diffusion couple method at 1 GPa and 1373-1573 K

- Below ΔFMQ +1, redox processes are controlled by O grain boundary diffusion, while above that, by H diffusion related with Mg vacancy

- Slow redox rate limits homogenization of subducted slab and mantle. A highly underestimated oxygen reservoir may be present in deep Earth.

Abstract

Redox input by subducting slab into deep mantle is of vital importance for deep cycle and isotopic evolution of volatile elements, whose chemically stable forms are controlled by redox state. Lithospheric mantle is crucial in redefining redox state of the Earth's deep mantle. To constrain to which extent subducted slab can modify redox state of the upper mantle and how much oxygen slab can carry into deep Earth, we investigated redox kinetics of olivine adopting diffusion couple methods at 1 GPa and 1373-1573 K in a piston cylinder apparatus. It is found that redox process in olivine is diffusion-controlled, and diffusing on the order of 10^{-12} m^2/s at 1473 K. The oxidation process in initially reduced olivine is oxygen fugacity (fO_2)-independent with activation enthalpy of 235±56 kJ/mol, while the reduction process in initially oxidized olivine is fO_2-dependent with an exponent of 2/5. Diffusion profile analysis reveals that redox state of starting material plays decisive role in determining redox mechanism. Below ΔFMQ+1, redox process in olivine is controlled by oxygen grain boundary diffusion, while above ΔFMQ+1, it is rate-limited by faster diffusion species which might be hydrogen related Mg vacancy. The extremely slow redox rate limits the homogenization of the slab and its surrounding mantle as redox state of the upper mantle remains unchanged for over past 3.5 Gyrs. The subducted slab has the ability to efficiently transport oxidized components to the region deeper than the mantle transition zone. A highly underestimated oxygen reservoir may have formed in the deep Earth.

Plain Language Summary

As oxidized slabs continue subducting into mantle, redox exchange occurs between slabs and the surrounding mantle. Knowledge of redox kinetics of olivine is essential for

understanding redox evolution of the uppermost mantle in the Earth's history. In this study, we conducted a series of diffusion couple experiments to determine rate of redox processes in olivine aggregates under high pressure and high temperature. Our results show that diffusion-controlled redox processes in olivine aggregates are extremely slow. The extent of surrounding mantle which can be oxidized by slab is very limited. The unchanging redox state of the uppermost mantle is not resulted from infinite redox capacity of the upper mantle as supposed but rather from its inability to digest oxidized components efficiently. Instead of fully absorbed by the upper mantle during subduction, the oxidized slabs can transport a considerable amount of oxidized components into the deep mantle.

Key words: redox kinetics, olivine, subducting slab, oxidation extent, redox budget, the upper mantle

1. Introduction

Evolution of redox state of the upper mantle through geological time has long been a focus of hot debate. Concentrations of Cr, V, and the V/Sc ratio of the oldest known rocks indicate that oxygen fugacity (fO_2) of the uppermost mantle has remained at approximately fayalite-magnetite-quartz (FMQ) over the past 3.5 Gyrs (Canil, 2002; Li and Lee, 2004). If mantle wedge is oxidized by subducted slab (Brounce et al., 2015; Parkinson and Arculus, 1999), it will prevent the incorporation of oxidized material into deep mantle. However, Zn/Fe_T signature in mantle wedge indicated that it is not originated from oxidized environment, which means that redox state of mantle wedge is not significantly altered by subduction of oxidized material (Lee et al., 2010). Oxidized arc rocks or gases originating

67 from mantle wedge is expected to bring dissolved oxidized components back to the Earth's

68 surface (Brounce et al., 2014; Kelley and Cottrell, 2009). However, $Fe^{3+}/\Sigma Fe$ ratios of

69 subducted materials of the Mariana subduction zone indicated that significant amount of

70 O_2 added to the subducted crust by several processes is not output by arc volcanism

71 (Brounce et al., 2019). Therefore, oxide components are likely to remain in the slab during

72 subduction, and transport into deeper mantle beyond subduction zones (Kadik, 1997;

73 Kasting et al., 1993). The unchanged fO_2 of the upper mantle remains to be a mystery.

74   The extent of mantle oxidized by subduction zone can be assessed by calculating input

75 and output of main redox-sensitive elements such as Fe, C and S (Evans, 2012; Evans and

76 Powell, 2015; Evans and Tomkins, 2011; Lécuyer and Ricard, 1999). Fe^{3+} flux from

77 sediments, altered oceanic crust and partially serpentinised lithospheric mantle is $15\pm$

78 13×10^{12} mole/y, which is ~27% of the total Fe flux (Evans, 2012). Redox budget of a rock

79 is defined as the number of moles of electrons which needs to be added to the rock to reach

80 a reference state (Evans, 2006). Fe is usually considered to be present in the form of Fe^{2+}

81 in the uppermost mantle. Thus, redox budget of Fe was calculated to be $15\pm13\times10^{12}$

82 mole/y, with respect to the reference state of Fe^{2+} (Evans, 2012). Therefore, contribution

83 of redox budget from C and S to deep mantle was increasingly investigated and emphasized

84 (Galvez et al., 2013; Kerrick and Connolly, 2001; Schwarzenbach et al., 2018; Sverjensky

85 et al., 2014) because of more electrons needed to bring them to reference states.

86   Net input of Fe (including Fe^{2+} and Fe^{3+}) is estimated to be $55\pm13\times10^{12}$ mole/y,

87 occupying up to 90% of multi-valence element fluxes. Ability of Fe in the slab as redox

88 budget is underestimated when we consider the fact that fO_2 decreases towards deep Earth

89 (Frost and McCammon, 2008). In the uppermost mantle, fO_2 is near FMQ equilibrium,

90 which is determined by Fe^{2+}-Fe^{3+} equilibria in silicate minerals. However, from lower half

91 of the upper mantle to the lower mantle, fO_2 decreases from near iron-wüstite (IW)

92 equilibrium to ~1.5 log units below that, producing metals with compositions from Ni-rich

93 to almost pure iron (Rohrbach and Schmidt, 2011). P-wave tomography revealed that most

94 of slabs stagnate above the 660 km discontinuity or trapped in the uppermost lower mantle

95 (600-1000 km), with some slabs penetrating the 660 km discontinuity or descending well

96 into the deep lower mantle (Fukao and Obayashi, 2013). It means that Fe in subducted slab

97 could be present in the form of metallic phase, at least partially, above the transition zone,

98 in order to maintain a dynamic equilibrium with surrounding reduced mantle whose fO_2 is

99 near IW and below. Thus, metallic iron should be referred as the reference state of Fe in

100 subducted slab above the transition zone. In this context, Fe flux (in the form of Fe^{2+}) from

101 unserpentinised lithospheric mantle which is usually 5-20 times thicker than serpentinised

102 one (Gorman et al., 2006; Rupke, 2004) should also be added to the net input of Fe

103 mentioned above. Otherwise, redox budget of Fe in slab would be further underestimated

104 when considering bulk volume of lithospheric mantle subducted to deep Earth every year.

105 Olivine and pyroxene are main constituent minerals in lithospheric mantle. When iron

106 in olivine is reduced to metallic phase during subduction, O_2 will be released and fO_2 of

107 surrounding mantle will be elevated. The hypothesis whether the upper mantle represents

108 an infinite redox reservoir and consumes all redox input supplied by slab so that a nearly

109 constant fO_2 of the upper mantle is maintained over geological time (Lee et al., 2010;

110 Rohrbach and Schmidt, 2011) should be examined. Experimental investigation on redox

111 kinetics of olivine is necessary, in order to accurately evaluate oxidation extent of the

112 surrounding mantle and redox budget of Fe brought by slab. In this study we employed

113   diffusion couple method to investigate redox kinetics of Pt-doped olivine aggregates (Pt as

114   oxygen sensor) at 1373-1573 K and 1 GPa under water undersaturated condition using

115   piston cylinder apparatus. Diffusion coefficient was calculated from fO_2 profile.

116   Mechanisms dominating reduction and oxidation processes are discussed. Assuming water

117   undersaturated condition, we calculate the maximum diffusion lengths through redox

118   processes and present the maximum oxidation extent of the upper mantle that can be altered

119   by the subducted slab. Finally, a total redox budget brought by slab into deep Earth every

120   year is estimated, taking metallic iron as the reference state.

121   **2. Methods**

122   **2.1 Sample preparation**

123   Reagent grade MgO, SiO_2 and Fe_2O_3 with stoichiometric olivine composition were

124   mixed in an agate mortar. 3 wt% SiO_2 powder was added as silica buffer. The powder

125   mixture was pressed into thin disks and baked at 1573 K in a gas mixture furnace for 4

126   hours with CO_2 and H_2 gas flow controlled at fO_2 near NNO (Ni-NiO) or IW buffered

127   condition. After baking, olivine was identified as the main phase with small amount of

128   orthopyroxene (Opx) using X-ray diffraction (XRD) analysis. Oxygen sensor of 5 wt% Pt

129   powder was added and fully mixed with pre-synthesized silica-buffered olivine powder,

130   which was baked at the same condition in the gas mixture furnace for 4 hours. After quench,

131   Pt-doped olivine powders at oxidized (near NNO buffer) and reduced (near IW buffer)

132   conditions were obtained.

133   Sintering of Pt-doped olivine aggregate was performed at 1373 to 1573 K, 1 GPa in

134   an end-loaded piston-cylinder apparatus using conventional 3/4" Talc/Pyrex assembly. To

135   obtain dry aggregate, starting powder was kept at 473 K in a vacuum furnace before it was

loaded into Ni or Mo capsule which was used for keeping the NNO or IW buffered condition of starting powders, respectively. To prevent generation of cracks by decompression, Pyrex glass tube was used outside Ni/Mo capsule and sample was decompressed to room pressure at 1073 K after sintering at the maximum temperature. After recovering the sample, the sintered sample was cut into several pieces. Microtexture was observed by scanning electron microscope (SEM) using a part of the sample.

Average grain size of olivine matrix was determined to be 24 μm (Supplementary Table S1), using intercept method (Mendelson, 1969) with a relation $D = cL$ where D is grain size, L is length of intercept, and c is a constant of 1.56. Volume fraction of Opx in olivine matrix was estimated using ImageJ on SEM images of the polished sample, which was 10–14 vol%. The increased amount of Opx is resulted from re-equilibrating of Pt particles with olivine during sintering, which causes breakdown of olivine into Fe and Opx, and release of oxygen, as indicated below:

$$Fe_2SiO_4 \text{ (olivine)} = 2Fe \text{ (metallic iron)} + SiO_2 + O_2 ; \qquad (1)$$

$$Mg_2SiO_4 + SiO_2 = 2MgSiO_3 . \qquad (2)$$
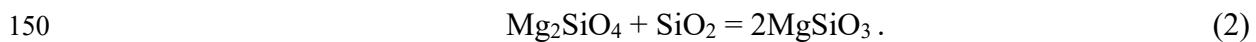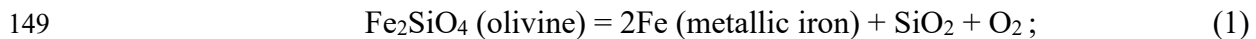
The absorbance of Fe by Pt particles allows fO_2 of sample to be evaluated (Faul et al., 2017).

To evaluate whether a new steady-state of fO_2 was reached, chemical composition of more than 20 points of Pt alloys and neighboring olivine grains from near Ni/Mo capsule to the center along cross section was measured by electron microprobe (EPMA) and their oxygen fugacities were calculated following previous method described in (Faul et al., 2017). The almost constant oxygen fugacity (Supplementary Fig. S1) indicates that sintered sample has reached a new equilibrium state corresponding to its sintering pressure and

159 temperature condition. For oxidized samples, except one sample containing significant

160 amount of magnetite which represents near 10 log units higher fO_2 than IW buffer, others

161 are magnetite-free and show oxygen fugacities 4.4–7.6 log units higher than IW buffer. fO_2

162 of the reduced samples was determined to be 1.1–1.6 log units higher than IW buffer

163 (Supplementary Table S1).

164 **2.2 Diffusion experiment and sample characterization**

165 To investigate diffusion-controlled redox kinetics, diffusion couple method was used.

166 After removing metal capsule from sintered samples, both oxidized and reduced Pt-doped

167 polycrystalline olivine disks with about 4 mm-diameter and 1 mm-thickness were surface-

168 polished and stacked face to face, referred as a diffusion couple. The couple was covered

169 with 10 μm thick Pt foil to avoid the reaction with surrounding MgO. Redox reaction is

170 expected to be driven progressively by fO_2 gradient across the contact interface. Diffusion

171 profile was confirmed to be absent in zero-time experiment in which experiment was

172 quenched by shutting down power supply once temperature increased to 1473 K. Time-

173 series diffusion experiments with different duration from 5 to 18 hours were performed at

174 1473 K, 1 GPa, the same temperature and pressure with their sintering conditions. To obtain

175 activation enthalpy, two additional experiments at 1373 and 1573 K were also performed

176 (Table 1).

177

178 **Table 1** Experimental summary of diffusion experiment using piston-cylinder apparatus

Run No.	Starting sample	T (K)	Duration (h)	Capsule	Grain size(μm)	Growth (%)	log D (m^2/s)
PC702	PC699+PC 686	1473	0	Pt foil	/	/	/
PC703	PC699+PC	1473	5	Pt foil	O: 4.5(2.5)	37	-12.20(8)

	686				R: 2.3(1.2)	2	
PC698	PC665+PC674	1473	13	Pt foil	O: 3.9(2.3)	26	-12.44(3)
					R: 3.1(1.7)	16	
PC715	PC714	1473	18	Pt foil	O: 4.8(3.0)	93	-12.64(2)
					R: 2.7(1.4)	15	
PC689*	PC687*+PC686	1473	12	Pt foil	/	/	-12.40(4)
					/	/	
PC711	PC710	1373	30	Pt foil	O: 2.5(1.4)	9	-12.97(4)
					R: 2.2(1.2)	-5	
PC719	PC718	1573	3	Pt foil	O: 4.2(2.3)	111	-11.83(4)
					R: 4.2(2.8)	14	

179

180   *magnetite-bearing sample or diffusion couple

181   "O" and "R" in the column of grain size mean oxidized half and reduced half of diffusion

182   couple respectively.

183   "-5" in column of Growth (%) means the grain size after diffusion experiment is the same

184   with that before diffusion experiment, i.e. no grain growth occurs.

185   Number in parenthesis is the calculated standard deviation of corresponding data.

186   "/" in PC702 and PC689 means corresponding properties is not calculated.

187

188   After annealing, diffusion couple was cut into two halves at center, normal to the

189   initial contact interface. One half of sample was used for SEM and EPMA measurement.

190   An interface between diffusion couple could be easily identified because of visible

191   separation by decompression, although two samples contacted well and their interfaces

192   were invisible (Fig. 1). A homogeneous texture with average grain size of 2–5 μm was

193   observed. In most cases no significant grain growth occurred (Table 1), neither obvious

194   change of volume fraction of orthopyroxene. Fe content in Pt alloy and chemical

195   composition of neighboring olivine across diffusion couple were acquired using EPMA

196 from the center part to minimize possible influence from outer Pt foil. Oxygen fugacity

197 profile was plotted as a function of distance from the initial contact interface (Fig. 2).

198   The other half of the recovered sample was double-polished to 100–300 μm thickness.

199 Water content was determined with a JASCO IRT5200IMPY Fourier-transform IR (FTIR)

200 spectrometer under vacuum and with an aligned transmission geometry. The spectra were

201 acquired with an aperture size of 100×100 and an accumulation of 128 scans. At least 3

202 to 5 different points were measured for each sample. After normalization for thickness and

203 correcting the baseline, the Paterson calibration (Paterson, 1982) was adopted with an

204 integration range of 3000–3730 cm^{-1} and an orientation factor of 1/2.

205 **2.3 Determination of diffusion coefficient**

206   Along diffusion profile, fO_2 gradient leads to chemical reaction between Pt oxygen

207 sensor and surrounding olivine grains until local equilibrium is reached. Iron content in

208 olivine grains is shown to be nearly constant (Supplementary Fig. S2). Whereas iron

209 content in Pt alloy (X_{Fe}) shows near linear relationship with fO_2 (Supplementary Fig. S3).

210 Thus, iron flux in Pt alloy (X_{Fe}) is a robust indicator to reflect fO_2 variation during redox

211

212

213
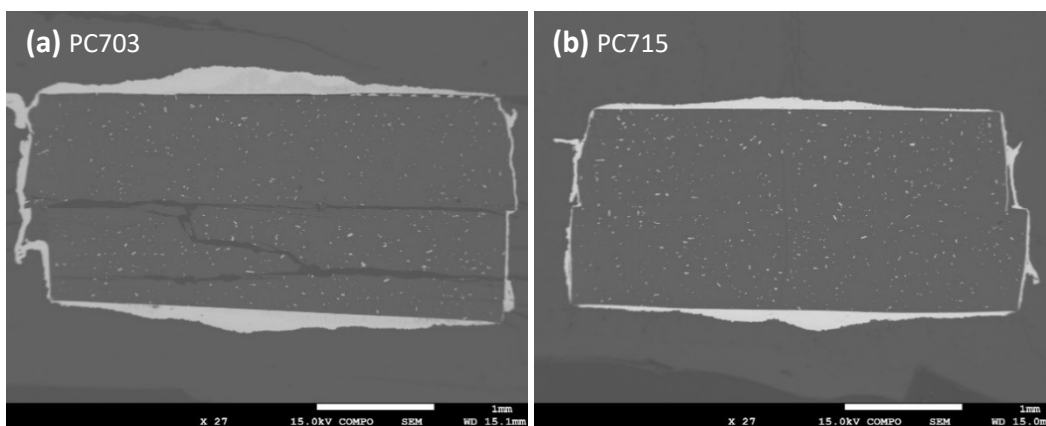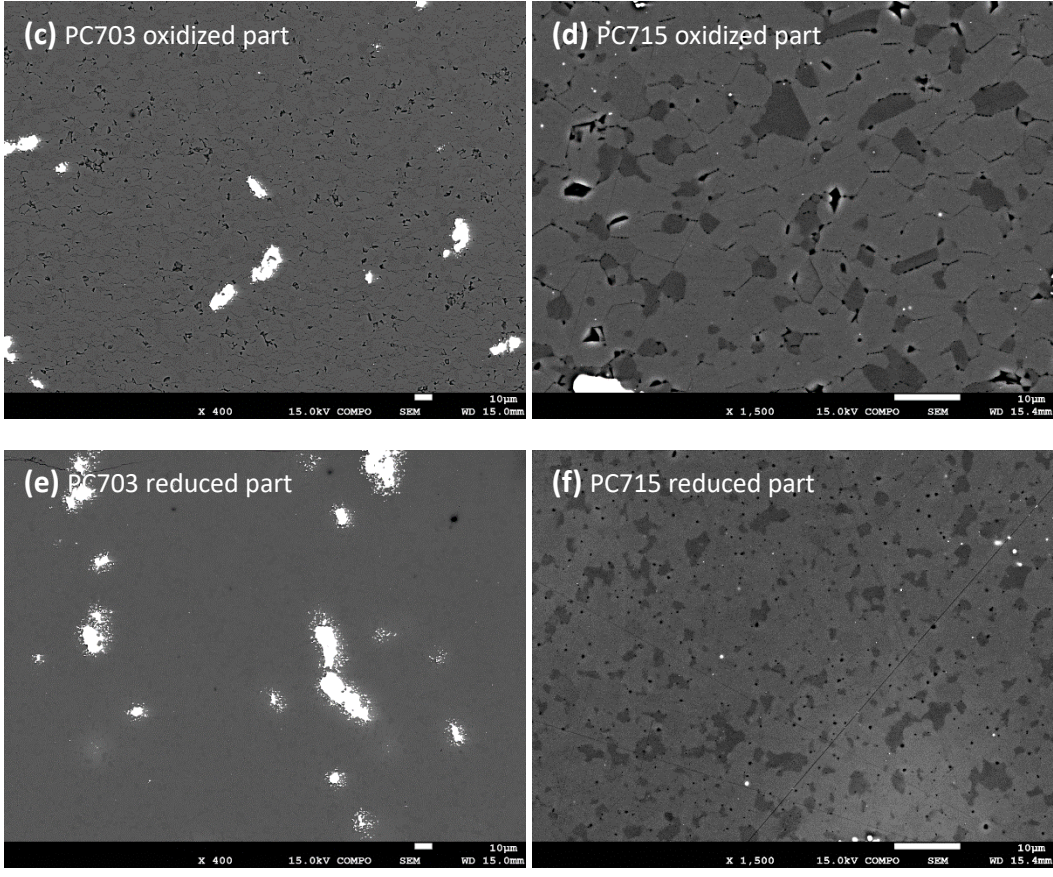
Fig. 1. Typical texture of diffusion couple after diffusion annealing with different durations at 1473 K. Volume fraction of orthopyroxene does not change much after annealing. Grain boundary in oxidized Pt-doped olivine aggregate becomes visible.

217

218

219
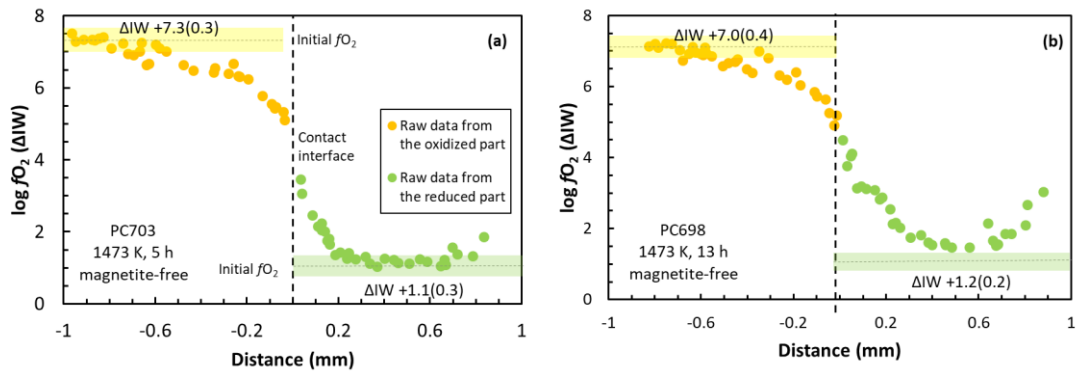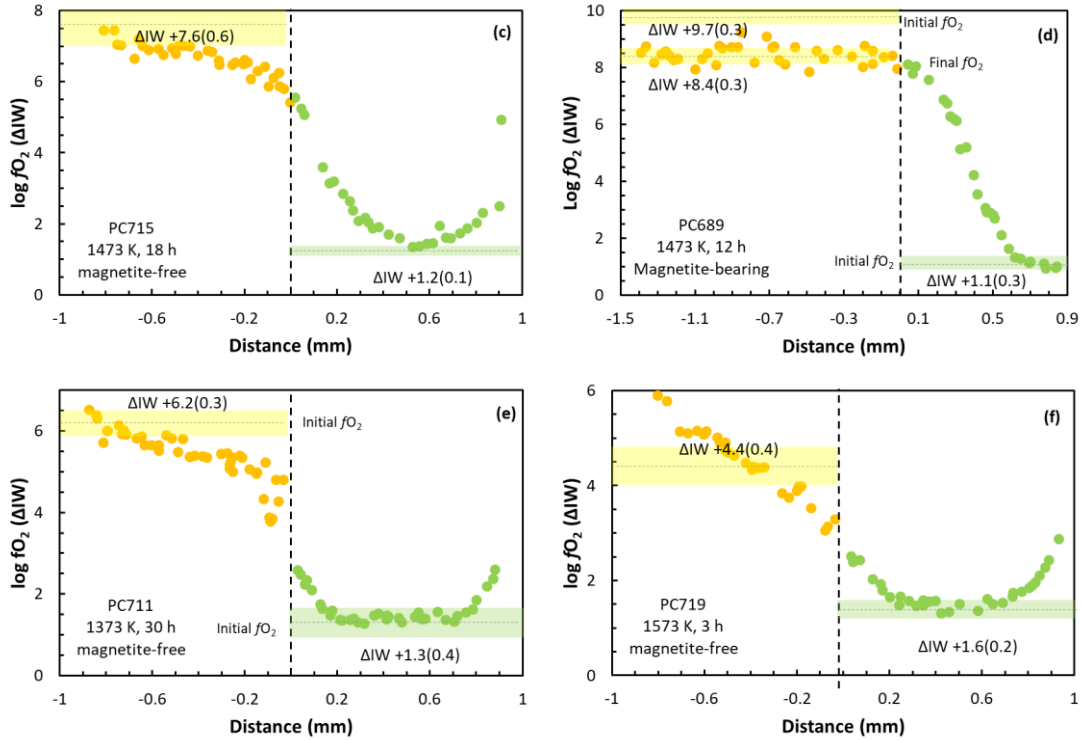
Fig. 2. Oxygen fugacity profiles as functions of distance from initial contact interface at 1373-1573 K. Yellow and green circles are fO_2 for oxidized and reduced part in diffusion couple respectively. Horizontal dotted lines are the initial fO_2 before diffusion. Yellow and green shaded areas are calculated standard deviation.

processes. To determine diffusion coefficients, redox process in olivine aggregate was assumed to be one-dimension diffusion in infinite space. After removing data points affected by Fe loss to the outer Pt foil, diffusion profiles of X_{Fe} in Pt alloy versus distance from the interface (Fig. 3) show asymmetric feature as a consequence of concentration-dependent diffusion coefficient. The boundary condition of semi-infinite media is satisfied when flat portion in diffusion profile suggests that the initial fO_2 condition was retained. Boltzmann-Matano method was used to obtain diffusion coefficient (Matano, 1933). First,

235 considering the asymmetric feature of diffusion profile, raw data was fitted to the equation

236 below:

$$C(x) = A_1 + (A_2 - A_1) \left[\frac{p}{1+10^{(Logx_1-x)h_1}} + \frac{1-p}{1+10^{(Logx_2-x)h_2}} \right] \qquad (3)$$

238 where x is the distance of data point from the initial interface, $C(x)$ is the mole fraction of

239 Fe in Pt alloy expressed as X_{Fe}, others are fitting parameters. After fitting, position of

240 Matano interface x was determined where it satisfied equation (5) below:

$$\int_{C_1}^{C_2} x dC = 0 \qquad (4)$$

242 where C_1 and C_2 are the minimum and maximum X_{Fe} in the diffusion profile, respectively.

243 Finally, diffusion coefficient was calculated using equation (6) below to obtain iron

244 content-dependent diffusivity:

$$D = -\frac{1}{2t} \left(\frac{dx}{dC} \right) \int_{C_1}^{C} x dC, \qquad (5)$$

246 where C is the normalized iron content at position x, D is the diffusion coefficient.

247 Although magnetite-bearing couple appears to be composition-independent,

248 Boltzmann-Matano method was also applied to determine the diffusion coefficient.

3. Results

250 Water contents of diffusion couples at 1373 and 1573 K are determined to be less than

251 10 wt. ppm. For diffusion couples at 1473 K, except one reduced sample whose water

252 content is within 10 wt. ppm, all others are between 20 and 50 wt. ppm (Supplementary

253 Fig. S4). Because of the difficulty to subtract water contribution from epoxy, the real water

254 contents of these samples are expected to be even lower. Therefore, it would be reasonable

255 to expect near dry condition for most couples during diffusion annealing.

256 Grain size of olivine in oxidized part of diffusion couple before diffusion usually is

comparable to or a little bit larger than that in reduced part, while for couple at 1573 K it is opposite (Supplementary Tables S1). After diffusion experiment, grain size of olivine in oxidized parts is 2.5–4.8 μm, with grain growth usually < 40% (Table 1). There are three couples whose grain growth reaches or exceeds 100%, indicating significant grain growth. For olivine in reduced part, grain size after diffusion is 2.2–4.8 μm, with grain growth < 20%. Therefore, there is no significant grain growth in reduced part during diffusion annealing. Grain boundaries in oxidized part are clear, while those in reduced part are invisible (Fig. 1).

0-time run demonstrates that there is no diffusion during heating up to the target temperature in both oxidized and reduced parts of the diffusion couple (Supplementary Fig. S5). fO_2 profiles as functions of distance from initial contact interface from 1373 to 1573 K (Fig. 2) indicate one-dimension asymmetric diffusion in infinite space. The initial fO_2 is maintained in both ends of diffusion couple. However, in run PC719, fO_2 in the oxidized part after diffusion is elevated by about 1.6 log units (Fig. 2f). It might be caused by oxidized atmosphere of the closed system trapped by Pt capsule. An upward tail is also frequently observed in reduced part which is due to loss of iron to Pt capsule.

Iron flux in Pt alloy (X_{Fe}) is a robust indicator to reflect fO_2 during diffusion process (Fig. 3). In the left side, X_{Fe} increases mildly over long distance (full length of sample

275

276

277
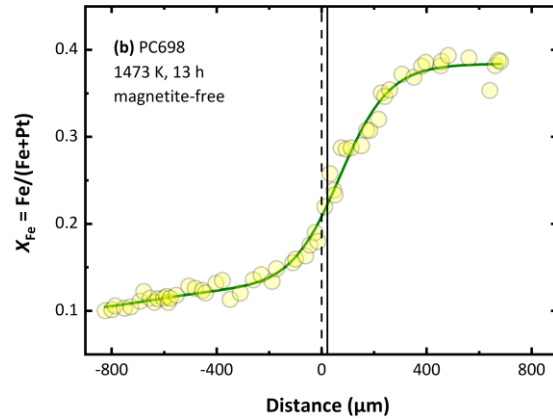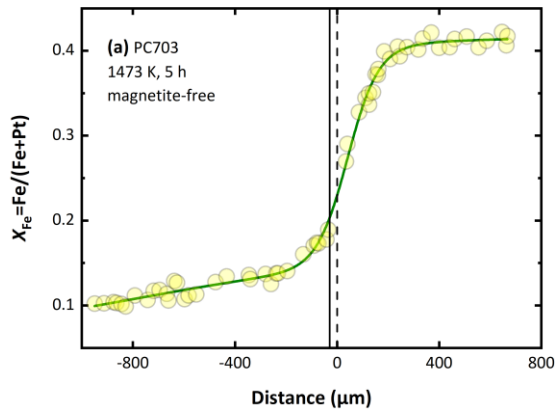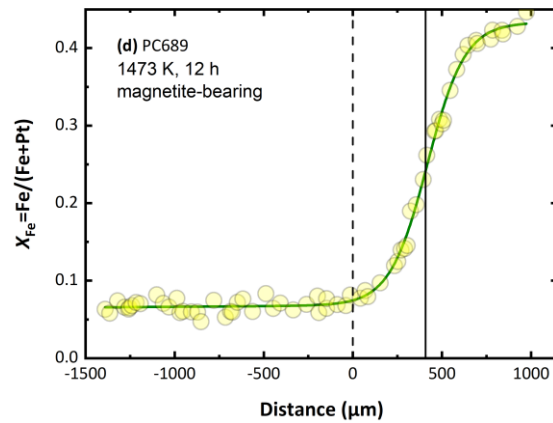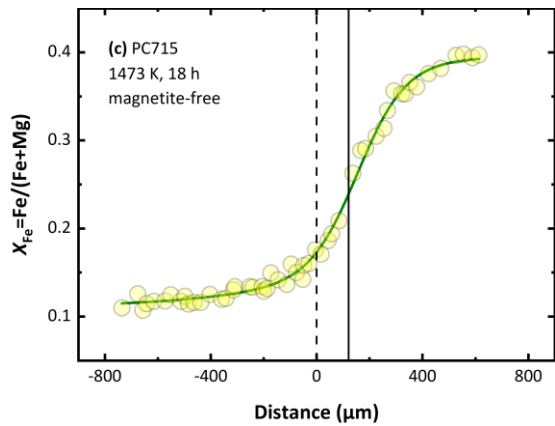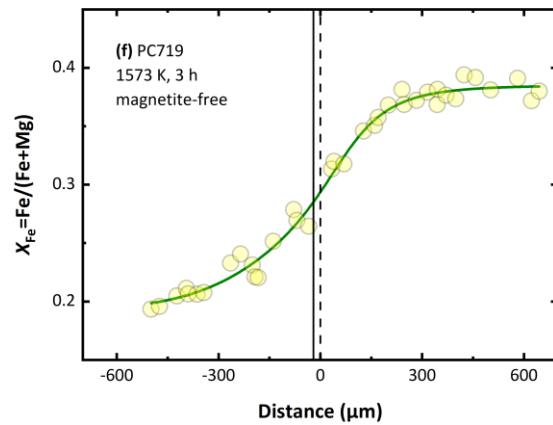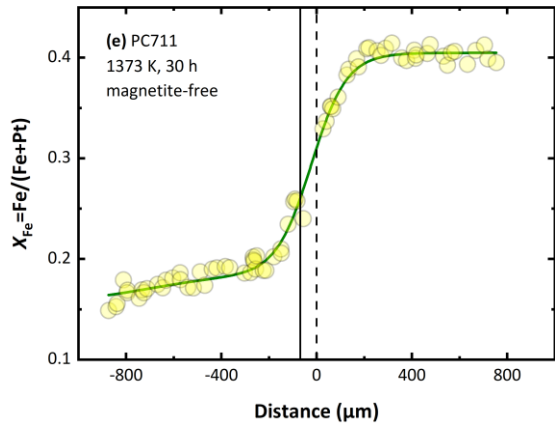
Fig. 3. Diffusion profile of iron content in Pt alloy (X_{Fe}) versus distance from the initial contact interface from 1373 to 1573 K with different durations. Yellow filled circles are iron mole fractions entrained in Pt alloy. Green line is the fitting line. Vertical dashed line indicates the initial contact interface and dashed line the Matano interface.

282

283 thickness), then increases steadily until the profile reaches its end and levels out in the right

284 side. Usually twice diffusion length was observed in the oxidized part. From fitting result

285 by Boltzmann-Matano method, time-series runs at 1473 K demonstrate that Matano

286 interface shifts to oxidized part at the beginning and then to reduced part with increased

287 duration. For diffusion couples annealed at 1373 and 1573 K, both Matano interfaces shift

288 to oxidized part. The direction shift of Matano interface might be caused by tilted diffusion

289 tail in oxidized part or inaccurate identification of the initial contact interface of diffusion

290 couple. Time-series runs annealed at 1473 K shows almost constant diffusivities within 4%

291 deviation (Supplementary Fig. S6).

292   Diffusion coefficients obtained against X_{Fe} show that diffusivity increases with

293 increasing temperature (Fig. 4). In magnetite-free couples, two different properties were

294 identified. In the reduced part where fO_2 is below Ni-NiO (NNO) buffer, diffusivity is

295 nearly constant, which is fO_2-independent. In the oxidized part, diffusivity increases with

296 decreasing X_{Fe}, which is fO_2-dependent. For fO_2-independent diffusion, average diffusion

297 coefficient was used (Table 1). Activation enthalpy (ΔH) is obtained (Fig. 5) through fitting

298 of diffusion coefficient (D) to the Arrhenius equation:

299 $$D = D_0 \exp\left(-\frac{\Delta H}{kT}\right),$$ (6)

300 where D_0 is pre-exponential factor, k is the Boltzmann constant, T is absolute temperature.

301 It yields $\Delta H = 235 \pm 56$ kJ/mol and $\log D_0 = -4.07 \pm 1.98$ m^2/s. For fO_2-dependent diffusion,

302 a linear relationship is found at 1473 K (dashed rectangle in Fig. 4) with the fO_2-exponent

303 p calculated to be 2/5 following the equation $D = D_0 f_{O_2}^p \exp\left(-\frac{\Delta H}{kT}\right)$.

304   In magnetite-bearing couple, diffusivity is fO_2-independent across the entire redox

305 range (Fig. 4). A symmetric fO_2 diffusion profile is completed within the reduced part (Fig.

306 2D). fO_2 in oxidized part lowered by 1.3 log units and no diffusion trend was observed in

307 the oxidized side. SEM observation revealed that magnetite corona enclosing Pt alloys

308 almost disappeared after diffusion annealing and the amount of small scattering magnetite

309 particles in matrix reduced significantly (Supplementary Fig. S7). Its diffusion coefficient

310 lies on the fitting line of magnetite-free couples (Fig. 5), which indicates the same redox

311 mechanism.

312
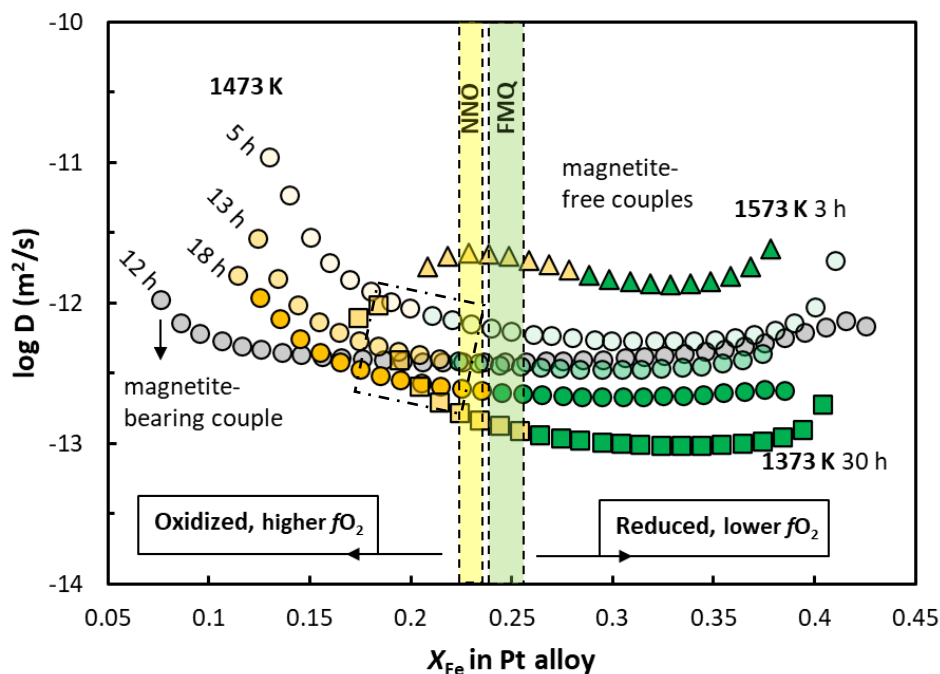
314 **Fig. 4.** Diffusion coefficient as a function of iron content in Pt alloy (X_{Fe}). Grey circles are

315 magnetite-bearing couple. Yellow and green symbols indicate original oxidized and

316 reduced part in magnetite-free couples respectively. Points in dash-dot rectangular are used

317 to calculate fO_2-exponent p.

318
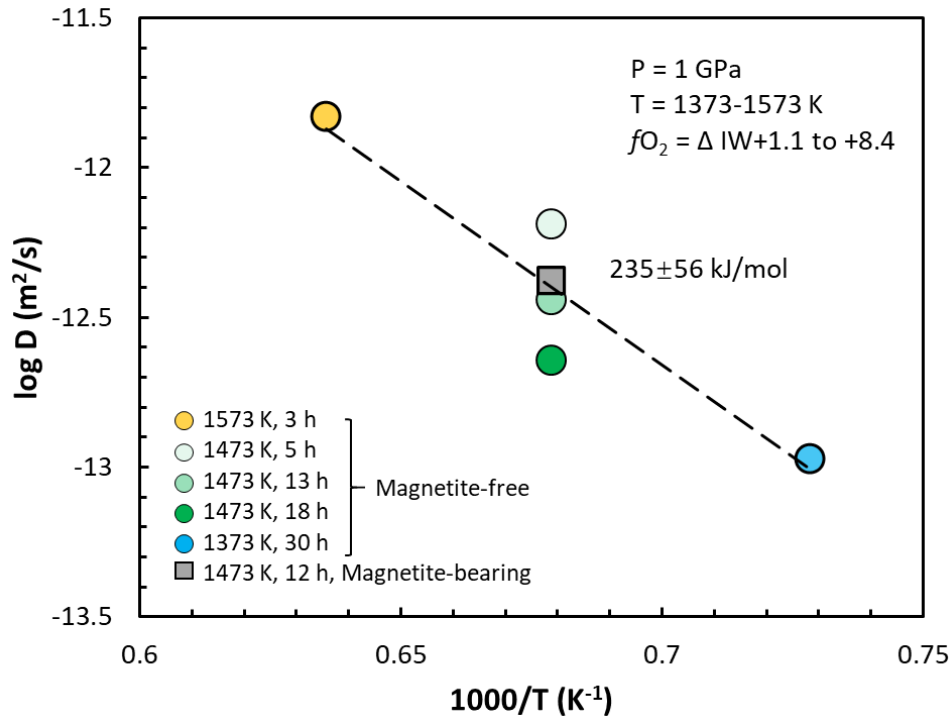
Fig. 5. Diffusion coefficient as a function of reciprocal temperature. Dashed black line is fitting line of diffusivity from magnetite-free couples.

4. Discussion

4.1 Redox mechanisms of olivine aggregates

Magnesium site in olivine is strongly incompatible to trivalent ions (e.g. Fe^{3+}) while more compatible to divalent ion with similar size of Mg^{2+} (e.g. Fe^{2+}). Thus, oxidized olivine with large amount of Fe^{3+} would be more sensitive to changing fO_2 due to its structural instability, which resulted in faster re-equilibrium during electrical conductivity and isothermal relaxation measurements (Ullrich and Becker, 2001; Wanamaker and Duba, 1993). The present study also demonstrates a four-times faster reduction rate in oxidized olivine that corresponds to 0.6 log unit difference in diffusivity (Fig. 4). Therefore, oxidation and reduction processes are governed by different mechanisms.

333   In this study, diffusion coefficients obtained at 1373–1573 K during oxidation process

334   are in the range of $10^{-11.5}$ to $10^{-13.5}$ m^2/s with ΔH of 235 ± 56 kJ/mol (Fig. 5). Because of

335   the apparent involvement of Fe and Mg, diffusivities of Fe-Mg interdiffusion in olivine

336   determined from previous studies are plotted for comparison (Fig. 6). ΔH averaged from

337   geometric mean value of three axes ranges from 177 to 301 kJ/mol (Dohmen et al., 2007;

338   Jurewicz and Watson, 1988; Nakamura and Schmalzried, 1984), which is similar to that in

339   this study. However, their diffusivities are 2.5 to 6 orders of magnitude lower. H_2O in

340   olivine was shown to increase interdiffusivity of Fe-Mg by approximately 1.5 orders (Hier-

341   Majumder, 2005). However, it is difficult to compensate for the large gap, given the

342   extremely low H_2O in the present study (Supplementary Fig. S4). Besides, factor of fO_2

343   dependence that is between 1/4 and 1/6 for Fe-Mg interdiffusion (Dohmen et al., 2007)

344   also contradicts with the fO_2-independent property in this study. Thus, Fe-Mg interdiffusion

345   is unfavorable for oxidation process.

346   Diffusivities of grain boundary diffusion (GBD) of O and Mg in forsterite are

347   comparable to that in oxidation process but show larger activation enthalpies (Fig. 6).

348   Magnesium GBD had high ΔH (376 kJ/mol) when trace amount of hydrogen existed

349   (Farver et al., 1994). In Arrhenius equation, similar pre-exponential factors relate to

350   comparable atomic jump distance or frequency, while different activation enthalpies

351   usually suggest different diffusion mechanisms. Thus Mg GBD can be ruled out as the

352   dominant mechanism for oxidation. For oxygen GBD in forsterite, the ΔH was determined

353   to be 367 ± 314 kJ/mol with significant error (Condit et al., 1985). When two abnormally

354   high diffusivities related to melt or penetration of oxygen along cracks were removed, the

355   other two points yield ΔH of 324 kJ/mol. When the effective grain boundary width is

356   corrected to 1 nm (Dohmen and Milke, 2010), the oxygen GBD in their study is on the

357   order of 10^{-12} m^2/s, consistent with diffusivity in oxidation process in this study.

358   Discrepancy of the activation enthalpy might be due to their extremely rare data points or

359   the absence of iron in their sample. Same order of diffusivity was also found for Fe loss

360   from San Carlos olivine to metal capsule which produced O_2 (Faul et al., 2017). Thus,

361   oxygen released from the oxidized part is expected to diffuse into the reduced part and

362   drives oxidation process through oxygen GBD.

363
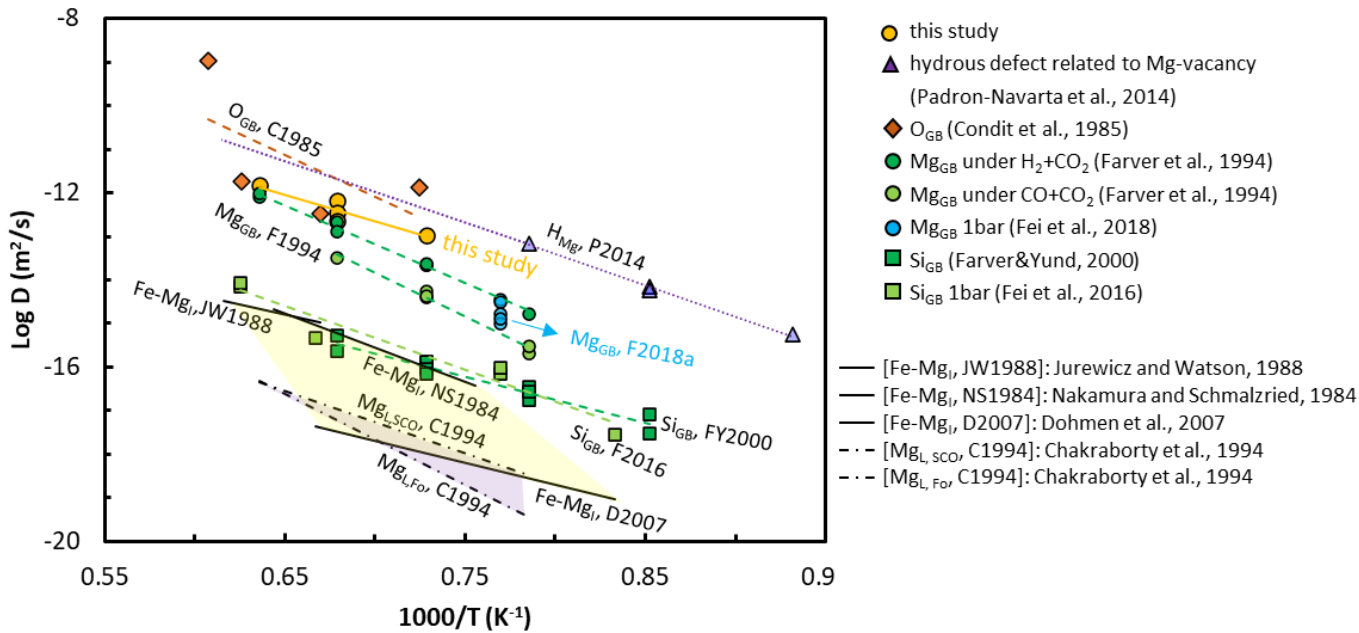
364

365   **Fig. 6.** Diffusion coefficient in oxidation process compared with those of other elements in

366   olivine. Yellowish region covers Fe-Mg interdiffusion in olivine and purplish region Mg

367   lattice diffusion. Except some data marked 1 GPa, others are obtained at room pressure.

368

369   For reduction process whose diffusivity is up to 0.6 log unit higher, its ΔH cannot be

370   determined from the present study. In the absence of solid graphite, CO and H_2 gas,

371   reduction process of San Carlos olivine could be controlled by diffusion in the bulk (Ullrich

372   and Becker, 2001). When the same mechanism is assumed in previous studies, ΔH in

373   previous studies exhibits a parabolic relationship with respect to forsterite content in

374   olivine (Fig. 7). It yields an estimated ΔH of ~250 kJ/mol for reduction of San Carlos

375   olivine (Fo_{92}). With elevated diffusivity compared with oxidation process, the possible

376   dominating diffusing species in reduction process might be hydrogen related with Mg

377   vacancy whose ΔH is about 274 kJ/mol (Padrón-Navarta et al., 2014). It was shown that

378   even the water content was extremely small on Mg site (< 10 wt. ppm), hydrous defects

379   related to Mg vacancy could diffuse on the order of $10^{-11.7}$ at 1473 K. The strong fO_2

380   dependence here could attribute to different site occupancies for hydrogen diffusing species

381   in order to meet charge neutrality conditions (Nishihara et al., 2008).

382   During reduction process in the oxidized olivine, released O_2 dissipates into its

383   counterpart through reaction $Fe_2SiO_4 = 2Fe + SiO_2 + O_2$ and metallic iron reduced from

384   fayalite fuses with platinum particle to form Fe-Pt alloy (Woodland and O'Neill, 1997).

385   The opening of grain boundary in oxidized sample after diffusion experiment might be

386   caused by opposition direction of reactions below (Faul et al., 2017):

387 $$3Fe_M^x + FeSiO_3 + 1/2\ O_2 = V_M'' + 2\ Fe_M^{\cdot} + Fe_2SiO_4 \tag{7}$$

388 $$Fe_M^x + Si_{Si}^x + 1/2\ O_2 + 1/2\ Fe_2SiO_4 = Fe_M^{\cdot} + Fe_{Si}' + 3/2SiO_2\ , \tag{8}$$
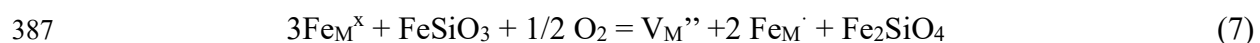
389   which minimize the concentration of metal vacancies, resulting in a slightly shrink of

390   crystal volume and thus visible grain boundaries (Fig. 1).

391   fO_2-dependent oxidation is also observed above NNO buffer at 1473 K, which

392   connects reduction process smoothly (Fig. 2a). This observation contradicts with fO_2-

393   independent diffusivity in oxidation of reduced olivine below FMQ buffer. It seems that

394 real-time fO_2 of olivine during diffusion annealing rather than the initial redox state plays

395 a vital role in determining redox mechanism. The cut-off point is around NNO buffer

396 (between ΔFMQ+0.5 and +1).

397

398
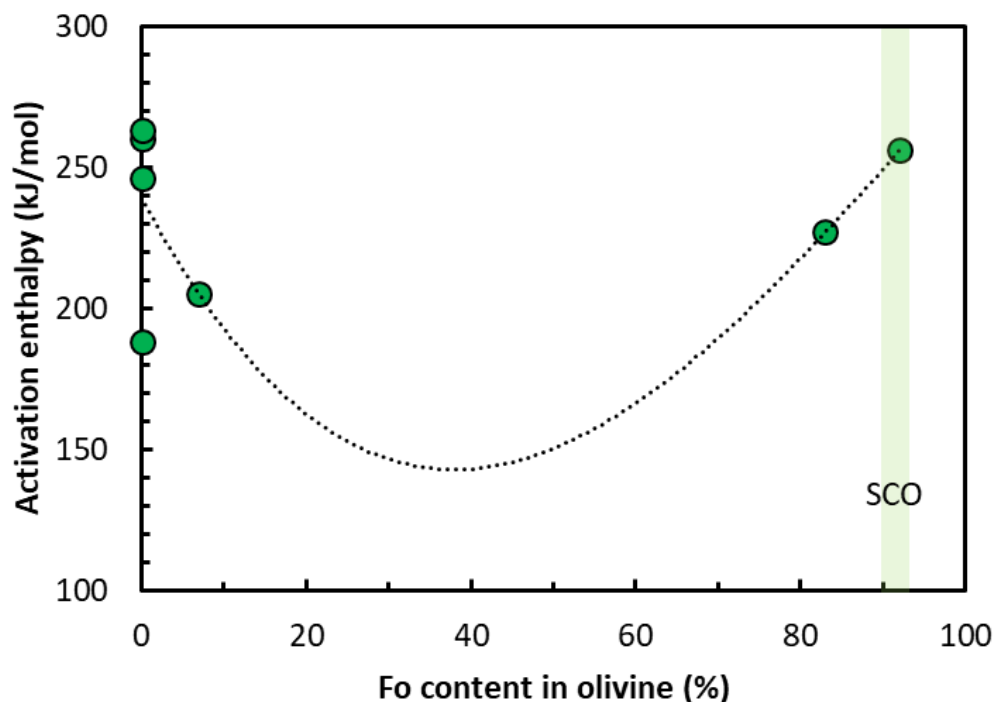
399 **Fig. 7.** ΔH of reduction process in olivine versus forsterite component from previous

400 studies. Dotted line is polynomial fitting of composition-dependent ΔH. Light green region

401 indicates ΔH of San Carlos olivine. For more detail, see supplementary materials.

402

403   In summary, redox process in olivine is controlled by oxygen GBD below ΔFMQ+1

404 buffer, while it is rate-limited by faster diffusion species which might be hydrogen related

405 Mg vacancy above ΔFMQ+1. As for the magnetite-bearing couple, the redox process might

406 be due to its infinite oxygen reservoir supplied by consumption of magnetite during

407 diffusion annealing. Thus, oxygen GBD controls oxidation process over wide range of fO_2

408   if magnetite exists.

4.2 Implications for oxidation extent of the upper mantle by slab and possible oxygen

budget in the deep Earth

Oxidized subducting slab has the ability to alter redox state of reducing mantle as an oxidant. However, its redox state as well as that of mantle wedge can be changed due to migration of fluids released by dehydration reactions at the initial stage of subduction. One index to evaluate redox state of slab and mantle wedge is Fe valence state. Chen et al. (2019) suggested that significant amount of Fe^{3+} in the mantle wedge was reduced to Fe^{2+} by reducing fluid derived from dehydration of serpentinite. On the contrary, some studies showed that dehydration of serpentinite can release more oxidized fluids (Debret et al., 2015; Evans et al., 2017), which played an opposite role to oxidize Fe^{2+}. At this moment, it is difficult to evaluate how much these dehydration reaction processes contribute to the redox budget of subducting slab. But even if we assume that the amount of Fe^{3+} reduced in slab outweighs that of Fe^{2+} oxidized, the extremely low solubility of Fe in NaCl solution (< 0.01 M) (Althaus and Johannes, 1969; Khodorevskaya and Aranovich, 2016; Wykes et al., 2008) makes the influence of such reactions on redox state of slabs negligible. Recent studies revealed that other multi-valence elements such as S and C are mostly retained within slab (Galvez et al., 2013; Piccoli et al., 2019), demonstrating little effect on the change of redox state of slab. Therefore, the subducted slab may maintain an oxidized state after the major dehydration process.

Spinel or garnet peridotite assemblages of xenoliths from subduction settings show fO_2 from ΔFMQ+1.5 to -1 (Frost and McCammon, 2008). fO_2 of surrounding upper mantle, which is mainly constituted by olivine, varies from FMQ equilibrium to ΔIW-1.5

431   (Rohrbach and Schmidt, 2011). Thus, there will be redox processes between the upper

432   mantle and subducting slab and the former will be oxidized by the latter through oxygen

433   GBD in olivine (see Discussion 4.1 for detail). Since slab continues subducting at steady

434   rate in the present Earth (Butterworth et al., 2014), the subducted slab can be considered as

435   an oxygen supplier with nearly constant oxygen fugacity which can continuously oxidize

436   the surrounding mantle. Oxidation extent of the upper mantle at certain depth can be

437   acquired by calculating diffusion length using the equation $L = 2\sqrt{Dt}$ where D is the

438   diffusion coefficient and t is the contact duration between mantle and subducting slab,

439   when temperature at that depth is known (Fig. 8). The effect of pressure on redox kinetics

440   was not considered. The oxygen GBD could have negative pressure dependence as well as

441   other elements in olivine (Farver et al., 1994; Fei et al., 2018). Thus, extrapolation of our

442   data to high pressure would yield the upper limit of oxidation length in the lowermost upper

443   mantle when temperature at the 410-seismic discontinuity was fixed at 1830 for the normal

444   mantle adiabat geotherm (Katsura et al., 2010). When slab passes through this depth for

445   100 Ma, only 462 m of the upper mantle can be oxidized. Even if slab starts subduction

446   and passing through the upper mantle for 4.5 Gyrs, the maximum diffusion length is less

447   than 4 km (Fig. 8). As surface temperature of real slab is much lower, diffusion processes

448   will contribute even less to the oxidation of reduced upper mantle under water-

449   undersaturated condition. This explains why $f\mathrm{O_2}$ of the upper mantle is rarely changed over

450   past 3.5 Ga (Canil, 2002; Li and Lee, 2004). Therefore, the unchanged $f\mathrm{O_2}$ of the uppermost

451   mantle in the past geological time is due to extremely sluggish redox process rather than

452   the speculation that mantle serves as an infinite redox buffer.
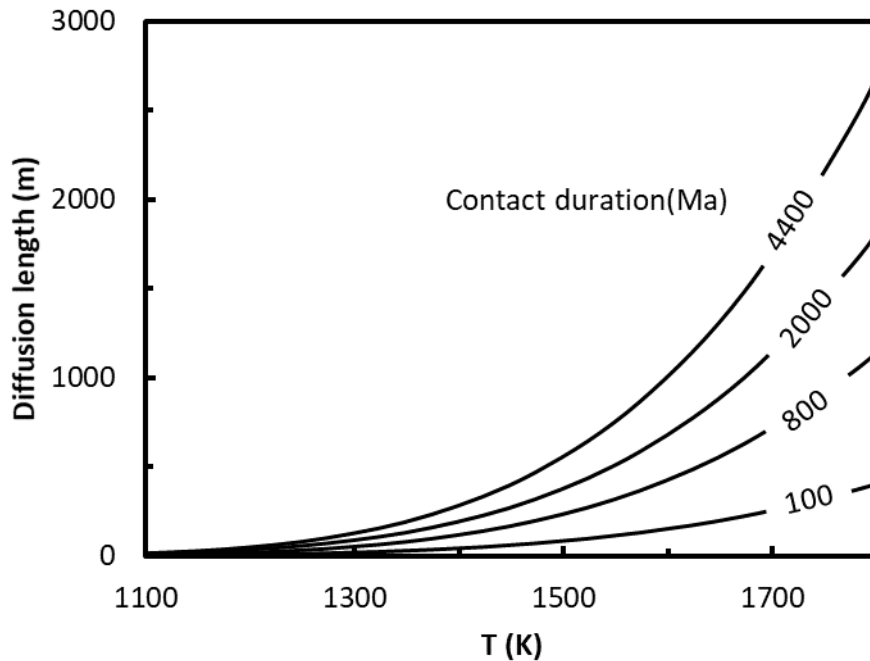
Fig. 8. Oxidation length of the upper mantle as a function of temperature (corresponding to geotherm at different depths). Numbers indicate the accumulative passing time of slab through the upper mantle.

Recent stratigraphic and geochemical studies suggested that some relics of subducted material operated 4.4 or 3.8 Gyrs ago (Turner et al., 2014). Episodic subduction till 2.1 Gyrs (Liu et al., 2019) and extremely dynamic mantle convective flow prevents slab from reaching deep Earth and renders redox process between deep upper mantle and subducting slab insufficient, which further decreases the diffusion length and redox budget in slab consumed by the upper mantle. Therefore, redox budget could be retained within slab fragments which results in contrastingly different fO_2 signatures observed in mid-ocean ridge basalts (MORBs) (Aeolus Lee et al., 2005; Bryndzia et al., 1989; Cottrell and Kelley, 2011), coupled with other geochemical signatures such as Os, Sr, Pb and Nd isotopes in

467   mantle heterogeneities due to slow diffusion processes (Kogiso et al., 2004).

468   The slow redox processes prevent subducting slab from being reduced, which

469   suggests that it can transport oxidized components to the mantle transition zone or the

470   lower mantle as an effective oxidant. To calculate the total redox budget brought by Fe in

471   slab, it is reasonable to define metallic phase as the reference since fO_2 in the deep upper

472   mantle is below IW equilibrium from beyond 8 GPa (~ 240 km) (Rohrbach and Schmidt,

473   2011). Assuming 1) total length of subduction zone is 44,450 km (Jarrard, 2003); 2)

474   average subduction rate is 13 mm/y (Butterworth et al., 2014); 3) olivine is the only

475   minerals in unserpentinised lithospheric mantle with Mg# equals to 90; 4) Fe^{3+} content in

476   olivine is negligible, Fe^{2+} flux in 100 km-thick unserpentinised lithospheric mantle is

477   calculated to be 156.4×10^{12} mol/y. Previous study showed that Fe^{3+} and Fe^{2+} fluxes from

478   sediments, crust and serpentinised lithosphere were 15×10^{12} and 39.6×10^{12} mol/y

479   respectively (Evans, 2012). Therefore, a total Fe^{2+} flux of 196×10^{12} mol/y and Fe^{3+} flux

480   of 15×10^{12} mol/y are obtained. Since metallic phase is defined as the reference state, both

481   Fe^{3+} and Fe^{2+} contribute to redox budget of Fe in slab. Redox budget is defined as the

482   number of moles of electrons needed to bring the rock to the reference state (Evans, 2006).

483   In the present study, it is the total amounts of electrons required to bring both Fe^{2+} and Fe^{3+}

484   to metallic phase, where 2 moles of electrons are required for Fe^{2+} and 3 moles for Fe^{3+}.

485   Therefore, total redox budget from Fe flux in slab is obtained as 437.1×10^{12} mol/y. It

486   gives the maximum amount of redox budget which slab can bring to deep Earth, which is

487   equivalent to 109.3×10^{12} mol/y oxygen gas (O_2). If minerals at the transition zone fails to

488   absorb most of oxidized components in slab, a highly underestimated oxygen reservoir

489   could be present in the lower mantle, as indicated by P-wave tomography that some slabs

490 descend well into the deep lower mantle (Fukao and obayashi., 2013). If oxidized

491 components reach the core-mantle boundary, it may contribute to negative tungsten

492 isotopes recorded by ocean island basalts (OIBs) such as Iceland and Hawaii (Mundl et al.,

493 2017; Yoshino et al., 2020).

5. Conclusions

495 We investigated redox kinetics of olivine adopting diffusion couple methods at 1 GPa,

496 1373-1573 K using piston cylinder apparatus. It is found that redox process in olivine is

497 diffusion-controlled, and diffusing on the order of 10^{-12} m^2/s at 1473 K. The oxidation

498 process in initially reduced olivine (IW buffered) is oxygen fugacity (fO_2)-independent

499 with activation enthalpy of 235±56 kJ/mol. The reduction process in initially oxidized

500 olivine (NNO buffered) is fO_2-dependent with an exponent of 2/5. Diffusion profile

501 analysis reveals that below ΔFMQ+1, redox process in olivine is controlled by oxygen

502 GBD, while above ΔFMQ+1, it is rate-limited by faster diffusion species which might be

503 hydrogen related Mg vacancy. For magnetite-bearing couple, diffusion profile only exists

504 in initially reduced part before running out of magnetite which might be due to that infinite

505 oxygen is supplied by consumption of magnetite in initially oxidized part during diffusion

506 annealing. Thus, oxygen GBD controls oxidation process in initially reduced sample over

507 wide range of fO_2.

508 Oxidation extent of the upper mantle at certain depth can be acquired by calculating

509 diffusion length. When slab passes through the lowermost upper mantle just above the

510 transition zone for 100 Ma, only 462 m of the surrounding mantle can be oxidized. Even if

511 slab starts subduction and passing through the upper mantle for 4.5 Gyrs, the maximum

512 diffusion length is less than 4 km. The extremely sluggish redox process explains why fO_2

513   of the upper mantle is rarely changed over past 3.5 Ga. Redox budgets could be retained

514   within slab fragments which results in contrastingly different fO$_2$ signatures observed in

515   mid-ocean ridge basalts. When slab subducts into lower mantle as indicated by P-wave

516   tomography, a highly underestimated oxygen reservoir can be formed if minerals at the

517   transition zone fails to absorb most of oxidized components in slab.

518

References

Althaus, E., Johannes, W., (1969), Experimental metamorphism of NaCl-bearing aqueous solutions by reactions with silicates. *American Journal of Science*, 267, 87-98.

Brounce, M., Cottrell, E., Kelley, K. A., (2019), The redox budget of the Mariana subduction zone. *Earth and Planetary Science Letters*, 528, 115859.

Brounce, M., Kelley, K. A., Cottrell, E., Reagan, M. K., (2015), Temporal evolution of mantle wedge oxygen fugacity during subduction initiation. *Geology*. 43, 775-778.

Brounce, M. N., Kelley, K. A., Cottrell, E., (2014), Variations in $Fe^{3+}/\Sigma Fe$ of Mariana arc basalts and mantle wedge fO_2. *Journal of Petrology*. 55, 2513-2536.

Bryndzia, L. T., Wood, B. J., Dick, H. J. B., (1989), The oxidation state of the Earth's sub-oceanic mantle from oxygen thermobarometry of abyssal spinel peridotites. *Nature*. 341, 526-527.

Butterworth, N. P., Talsma, A. S., Müller, R. D., Seton, M., Bunge, H. P., Schuberth, B. S. A., Shephard, G. E., Heine, C., (2014), Geological, tomographic, kinematic and geodynamic constraints on the dynamics of sinking slabs. *Journal of Geodynamics*. 73, 1-13.

Canil, D., (2002), Vanadium in peridotites, mantle redox and tectonic environments:

543   Archean to present. *Earth and Planetary Science Letters*. 195, 75-90.

544   Chakraborty, S., Farver, J. R., Yund, R. A., Rubie, D. C., (1994), Mg tracer diffusion in

545   synthetic forsterite and as a function of P, T and fO_2. *Physics and Chemistry of Minerals*.

546   21, 489-500.

547   Chen, Y.-X., Lu, W., He, Y., Schertl, H.-P., Zheng, Y.-F., Xiong, J.-W., Zhou, K., (2019),

548   Tracking Fe mobility and Fe speciation in subduction zone fluids at the slab-mantle

549   interface in a subduction channel: A tale of whiteschist from the Western Alps. *Geochimica*

550   *et Cosmochimica Acta*. 267, 1-16.

551   Condit, R. H., Weed, H. C., Piwinskii, A. J., (1985), A technique for observing oxygen

552   diffusion along grain boundary regions in synthetic forsterite. In Schock. R.N. (ed.) *Point*

553   *Defects in Minerals, Geophysical Monograph Series* (vol. 31, pp. 97-105). Washington,

554   DC: American Geophysical Union.

555   Cottrell, E., Kelley, K. A., (2011), The oxidation state of Fe in MORB glasses and the

556   oxygen fugacity of the upper mantle. *Earth and Planetary Science Letters*. 305, 270-282.

557   Debret, B., Bolfan-Casanova, N., Padrón-Navarta, J. A., Martin-Hernandez, F., Andreani,

558   M., Garrido, C. J., et al. (2015), Redox state of iron during high-pressure serpentinite

559   dehydration. *Contributions to Mineralogy and Petrology*. 169, 36.

560   Debret, B., Millet, M.-A., Pons, M.-L., Bouilhol, P., Inglis, E., Williams, H., (2016),

561   Isotopic evidence for iron mobility during subduction. *Geology*. 44, 215-218.

562   Dohmen, R., Becker, H.-W., Chakraborty, S., (2007), Fe-Mg diffusion in olivine I:

563   Experimental determination between 700 and 1,200°C as a function of composition, crystal

564   orientation and oxygen fugacity. *Physics and Chemistry of Minerals*. 34, 389-407.

565   Dohmen, R., Milke, R., (2010), Diffusion in polycrystalline materials: Grain boundaries,

mathematical models, and experimental data. *Reviews in Mineralogy and Geochemistry*. 72, 921-970.

Evans, K. A., (2006), Redox decoupling and redox budgets: Conceptual tools for the study of earth systems. *Geology*. 34, 489-492.

Evans, K. A., (2012), The redox budget of subduction zones. *Earth-Science Reviews*. 113, 11-32.

Evans, K. A., Powell, R., (2015), The effect of subduction on the sulphur, carbon and redox budget of lithospheric mantle. *Journal of Metamorphic Geology*. 33, 649-670.

Evans, K. A., Reddy, S. M., Tomkins, A. G., Crossley, R. J., Frost, B. R., (2017), Effects of geodynamic setting on the redox state of fluids released by subducted mantle lithosphere. *Lithos*. 278-281, 26-42.

Evans, K. A., Tomkins, A. G., (2011), The relationship between subduction zone redox budget and arc magma fertility. *Earth and Planetary Science Letters*. 308, 401-409.

Farver, J. R., Yund, R. A., (2000), Silicon diffusion in forsterite aggregates: Implications for diffusion accommodated creep. *Geophysical Research Letters*. 27(15), 2337-2340.

Farver, J. R., Yund, R. A., Rubie, D. C., (1994), Magnesium grain boundary diffusion in forsterite aggregates at 1000°-1300°C and 0.1 MPa to 10 GPa. *Journal of Geophysical Research*. 99(B10), 19809-19819.

Faul, U. H., Cline II, C. J., Berry, A., Jackson, I., Garapić, G., (2017), Constraints on oxygen fugacity within metal capsules. *Physics and Chemistry of Minerals*. https://doi.org/10.1007/s00269-017-0937-7.

Fei, H., Koizumi, S., Sakamoto, N., Hashiguchi, M., Yurimoto, H., Marquardt, K., et al. (2018), Pressure, temperature, water content, and oxygen fugacity dependence of the Mg

grain-boundary diffusion coefficient in forsterite. *American Mineralogist*. 103, 1354-1361.

Fei, H., Koizumi, S., Sakamoto, N., Hashiguchi, M., Yurimoto, H., Marquardt, K., et al. (2016), New constraints on upper mantle creep mechanism inferred from silicon grain-boundary diffusion rates. *Earth and Planetary Science Letters*. 433, 350-359.

Frost, D. J., McCammon, C. A., 2008. The Redox State of Earth's Mantle. *Annual Review of Earth and Planetary Sciences*. 36, 389-420.

Fukao, Y., Obayashi, M., 2013. Subducted slabs stagnant above, penetrating through, and trapped below the 660 km discontinuity. *Journal of Geophysical Research*. 118, 5920-5938.

Galvez, M. E., Beyssac, O., Martinez, I., Benzerara, K., Chaduteau, C., Malvoisin, B., et al. (2013), Graphite formation by carbonate reduction during subduction. *Nature Geoscience*. 6, 473-477.

Gorman, P. J., Kerrick, D. M., Connolly, J. A. D., (2006), Modeling open system metamorphic decarbonation of subducting slabs. Geochemistry, Geophysics, Geosystems. 7(4), doi:10.1029/2005GC001125

Hier-Majumder, S., Anderson, I. M., Kohlstedt, D. L., (2005), Influence of protons on Fe-Mg interdiffusion in olivine. *Journal of Geophysical Research*. 110(B02202), doi:10.1029/2004JB003292

Jarrard, R. D., (2003), Subduction fluxes of water, carbon dioxide, chlorine, and potassium. *Geochemistry, Geophysics, Geosystems*. 4(5), doi:10.1029/2002GC000392

Jurewicz, A. J. G., Watson, E. B., (1988), Cations in olivine, Part 2: Diffusion in olivine xenocrysts, with applications to petrology and mineral physics. *Contributions to Mineralogy and Petrology*. 99, 186-201.

Katsura, T., Yoneda, A., Yamazaki, D., Yoshino, T., Ito, E., (2010), Adiabatic temperature

612   profile in the mantle. *Physics of the Earth and Planetary Interiors*. 183, 212-218.

613   Kelley, K. A., Cottrell, E., (2009), Water and the oxidation state of subduction zone

614   magmas. *Science*. 325, 605-607.

615   Kerrick, D. M., Connolly, J. A. D., (2001), Metamorphic devolatilization of subducted

616   marine sediments and the transport of volatiles into the Earth's mantle. *Nature*. 411, 293-

617   296.

618   Khodorevskaya, L. I., Aranovich, L. Y., (2016), Experimental study of amphibole

619   interaction with H_2O-NaCl Fluid at 900°C, 500 MPa: Toward granulite facies melting and

620   mass transfer. *Petrology*. 24(3), 235-254.

621   Kogiso, T., Hirschmann, M. M., Reiners, P. W., (2004), Length scales of mantle

622   heterogeneities and their relationship to ocean island basalt geochemistry. Geochimica et

623   Cosmochimica Acta. 68(2), 345-360.

624   Lécuyer, C., Ricard, Y., (1999), Long-term fluxes and budget of ferric iron: implication for

625   the redox states of the Earth's mantle and atmosphere. *Earth and Planetary Science Letters*.

626   165, 197-211.

627   Lee, C.-T. A., Luffi, P., Le Roux, V., Dasgupta, R., Albarede, F., Leeman, W. P., (2010),

628   The redox state of arc mantle using Zn/Fe systematics. *Nature*. 468, 681-685.

629   Lee, C.-T. A., Leeman, W. P., Canil, D., Li, Z.-X. A., (2005), Similar V/Sc systematics in

630   MORB and arc basalts: Implications for the oxygen fugacities of their mantle source

631   regions. *Journal of Petrology*, 46(11), 2313-2336.

632   Li, Z.-X. A., Lee, C.-T. A., 2004. The constancy of upper mantle fO_2 through time inferred

633   from V/Sc ratios in basalts. *Earth and Planetary Science Letters*. 228, 483-493.

634   Liu, H., Sun, W. D., Zartman, R., Tang, M., (2019), Continuous plate subduction marked

by the rise of alkali magmatism 2.1 billion years ago. *Nature Communication*. 10, 3408.

https://doi.org/10.1038/s41467-019-11329-z

Matano, C., (1933), On the relation between the diffusion coefficients and concentrations

of solid metals (the nickel-copper system). *Japanese Journal of Physics*. 8, 109-113.

Mendelson, M.I., (1969), Average grain size in polycrystalline ceramics. *Journal of The*

American Ceramic Society. 52(8), 443-446.

Mundl, A., Touboul, M., Jackson, M. G., Day, J. M. D., Kurz, M. D., Lekic, V., et al. (2017),

Tungsten-182 heterogeneity in modern ocean island basalts. *Science*. 356, 66-69.

Nakamura, A., Schmalzried, H., (1984), On the Fe^{2+}-Mg^{2+}-interdiffusion in olivine (II).

Berichte der Bunsengesellschaft für physikalische Chemie. 88, 140-145.

Nishihara, Y., Shinmei, T., Karato, S.-I., (2008). Effect of chemical environment on the

hydrogen-related defect chemistry in wadsleyite. *American Mineralogist*. 93, 831-843.

Padrón-Navarta, J. A., Hermann, J., O'Neill, H. S. C., (2014), Site-specific hydrogen

diffusion rates in forsterite. *Earth and Planetary Science Letters*. 392, 100-112.

Parkinson, I. J., Arculus, R. J., (1999), The redox state of subduction zones: Insights from

arc-peridotites. *Chemical Geology*. 160, 409-423.

Paterson, M. S., (1982), The determination of hydroxyl by infrared absorption in quartz,

silicate glasses and similar materials. *Bull. Mineral*. 105, 20-29.

Piccoli, F., Hermann, J., Pettke, T., Connolly, J. A. D., Kempf, E. D., Duarte, J. F. V., (2019),

Subducting serpentinites release reduced, not oxidized, aeueous fluids. *Scientific Reports*.

9, 19573. https://doi.org/10.1038/s41598-019-55944-8

Rohrbach, A., Schmidt, M. W., 2011. Redox freezing and melting in the Earth's deep mantle

resulting from carbon-iron redox coupling. *Nature*. 472, 209-212.

658   Rupke, L. H., Morgan, J. P., Hort, M., Connolly, J. A. D., (2004), Serpentine and the

659   subduction zone water cycle. *Earth and Planetary Science Letters*. 223, 17-34.

660   Schwarzenbach, E. M., Caddick, M. J., Petroff, M., Gill, B. C., Cooperdock, E. H. G.,

661   Barnes, J. D., (2018), Sulphur and carbon cycling in the subduction zone melange.

662   Scientific Report. 8, 15517. DOI:10.1038/s41598-018-33610-9

663   Sverjensky, D. A., Stagno, V., Huang, F., (2014), Important role for organic carbon in

664   subduction-zone fluids in the deep carbon cycle. *Nature Geoscience*. DOI:

665   10.1038/NGEO2291

666   Turner, S., Rushmer, T., Reagan, M., Moyen, J. F., (2014), Heading down early on? Start

667   of subduction on Earth. *Geology*. doi:10.1130/G34886.1

668   Ullrich, K., Becker, K. D., (2001), Kinetics and diffusion of defects in fayalite, Fe_2SiO_4.

669   *Solid State Ionics*. 141-142, 307-312.

670   Wanamaker, B. J., Duba, A. G., (1993), Electrical conductivity of San Carlos Olivine along

671   [100] under oxygen- and pyroxene-buffered conditions and implications for defect

672   equilibria. *Journal of Geophysical Research*. 98(B1), 489-500.

673   Woodland, A. B., O'Neill, H. S. C., 1997. Thermodynamic data for Fe-bearing phases

674   obtained using noble metal alloys as redox sensors. *Geochimica et Cosmochimica Acta*.

675   61(20), 4359-4366.

676   Wykes, J. L., Newton, R. C., Manning, C. E., (2008), Solubility of andradite, $Ca_3Fe_2Si_3O_{12}$,

677   in a 10 mol% NaCl solution at 800 ºC and 10 kbar: Implications for the metasomatic origin

678   of grandite garnet in calc-silicate granulites. *American Mineralogist*. 93, 886-892.

679   Yoshino, T., Makino, Y., Suzuki, T., Hirata, T., (2020), Grain boundary diffusion of W in

680   lower mantle phase with implications for isotopic heterogeneity in oceanic island basalts

681 by core-mantle interactions. *Earth and Planetary Science Letters*. 530.

682 https://doi.org/10.1016/j.epsl.2019.115887

683

684

685

686

687

688

689

690

691

692

693

694

695

696

697

698

699

700

701

702

703

704

705

706

707

708

709

710

711

712

713

714

715

716

717

718

719

720

721

722

723

724

725

726

727

728

Supplementary Materials

Title: Oxygen budget in Earth's mantle inferred from redox kinetics of olivine

Chengcheng Zhao [1]* †, Takashi Yoshino[1], Baohua Zhang[2]

[1] Institute for Planetary Materials, Okayama University, Misasa, Tottori 682-0193, Japan.

[2] Key Laboratory of Geoscience Big Data and Deep Resource of Zhejiang Province,

Institute of Geology and Geophysics, School of Earth Sciences, Zhejiang University,

Hangzhou 310027, China.

† Current address: Laboratoire Magmas et Volcans CNRS, IRD, OPGC, Université

Clermont Auvergne, 63000 Clermont-Ferrand, France

* Corresponding author. E-mail addresses: cczhao_zhao@outlook.com

1. The effect of iron loss, grain size, grain growth and grain boundary on diffusion coefficient

Asymmetric diffusion highlights in $f\!O_2$ as a function of distance from initial contact interface (Fig. 2), which results in X_{Fe}-dependent diffusion coefficient in the oxidized part of diffusion couple (Fig. 4). X_{Fe} in Pt alloy is a visualized indicator of $f\!O_2$, it corresponds to $f\!O_2$-dependent redox process. Although significant iron loss to Pt capsule occurs in reduced part which is shown as an upward bending tail, the flattening end in the oxidized counterpart implies that the initial oxygen fugacity was held constant during diffusion annealing and iron loss to Pt capsule is negligible (Fig. 2). Thus $f\!O_2$-dependent diffusivity could not be an artifact of iron loss.

Grain size contrast might be the driving force to introduce asymmetric and X_{Fe}-dependent diffusion. Average grain sizes of olivine matrix between oxidized and reduced parts before diffusion are almost the same except one couple at 1573 K whose olivine size in oxidized part is doubled (Supplementary Table S1). After diffusion annealing, olivine grain size increased congruously within diffusion couples with two exceptions which show doubled grain size in the oxidized part at 1473 K and 1573 K respectively (Table 1). If grain size contrast within diffusion couple induces asymmetric diffusion profile, faster diffusivity in the reduced part would appear since grain boundary proportion in finer-grained reduced part increases which is proved to enhance diffusion process by several orders of magnitude (Dohmen and Milke, 2010; Farver et al., 1994; Fei et al., 2018). However, this possibility is precluded since oxidized parts in the present study always show larger diffusion coefficients and diffusion couples with different grain size contrasts at 1473 K have similar dependence of diffusion coefficient on X_{Fe} (Fig. 4).

40　Influence of grain growth during diffusion annealing is also evaluated. After diffusion

41　annealing at 1473 K, the reduced part underwent limited grain growth within 15%, while

42　for the oxidized part, extent of grain growth varied from 15 to 90% (Supplementary Table

43　1). If grain growth were to affect diffusion process, larger grain growth contrast within

44　diffusion couple might exhibit more obvious asymmetric property. However, the near

45　parallel slope shown for grain growth contrast from one to six times also rules out this

46　possibility (Fig. 4).

47　　Having noticed the appearance of clearly visible grain boundary in oxidized part of

48　diffusion couple after annealing which is invisible in its reduced counterpart (Fig. 1),

49　whether high fO$_2$ in the oxidized sample leads to the opening of grain boundary and results

50　in elevated diffusivity becomes a question. Contrary to magnetite-free couples, a

51　symmetric and complete diffusion profile was obtained within the reduced part of

52　magnetite-bearing diffusion couple (Fig. 2d), demonstrating X_{Fe}-independent nature across

53　wide fO$_2$ range (Fig. 4). SEM observation reveals that high fO$_2$ in the environment does

54　not lead to visible grain boundary as expected (Fig. S7). Furthermore, the fact that

55　magnetite-bearing diffusion couple gives consistent diffusivity with others (Fig. 4)

56　suggests negligible influence of grain boundary effect on redox process.

57　　During reduction process in the oxidized olivine, released oxygen dissipates into its

58　counterpart through reaction Fe$_2$SiO$_4$ = 2Fe + SiO$_2$ + O$_2$ and metallic iron reduced from

59　fayalite fuses with platinum particle to form Fe-Pt alloy (Faul et al., 2017; Woodland and

60　O'Neill, 1997). The opening of grain boundary in oxidized sample after diffusion

61　experiment might be caused by opposition direction of reactions (1) and (2) which

62　minimize the concentration of metal vacancies and lead to a slightly shrink of crystal

63   volume and resultant visible grain boundary (Fig. 1) (Massieon et al., 1993).

64   Edge effect from Boltzmann-Matano method could be up to 0.4 log unit according to its

65   up-bending tails (Fig. 4). Thus, a dependence of about 0.6 log unit of diffusion coefficient

66   on X_{Fe} is estimated for oxidized sample in all diffusion couples.

67 **2. Summary of previous studies on redox kinetics in olivine at ambient pressure**

68   Oxidation process was mostly investigated at low temperature in previous studies. A

69   linear rate law of increasing thickness of oxidized layer or Fe^{3+} fraction was found for first

70   stage of oxidation of fine-grained olivine (Fo_{89}) at 873-973 K in air with ΔH of 73 kJ/mol

71   which formed ferrifayalite (Khisina et al., 1998; Khisina et al., 1995), and for oxidation of

72   fayalite single crystal at 1303 K using CO/CO_2 gas mixture within magnetite stability

73   (Mackwell, 1992). On the other hand, a parabolic rate law was determined for second stage

74   of oxidation with activation enthalpy of 118 kJ/mol which formed magnesioferrite plus

75   silica (Khisina et al., 1998; Khisina et al., 1995), and for oxidation of olivine single crystal

76   Fo_{90} in air between 973 and 1373 K with ΔH of 140 kJ/mol (Wu and Kohlstedt, 1988) and

77   of fayalite single crystal in air at 1043 K (Mackwell, 1992). Thus, it seems that progress of

78   oxidation status, species of gas media and temperature could influence dominant rate-

79   limiting process since linear rate law can be regarded as interface-controlled reaction while

80   parabolic rate law indicating diffusion-controlled process (Khisina et al., 1998; Khisina et

81   al., 1995; Mackwell, 1992).

82   Previous studies yielded ΔH of 246-263 kJ/mol for reducing fayalite at 1523-1723 K and

83   1073-1373 K using H_2+CO or H_2 or graphite (Gaballah et al., 1975; Massieon et al., 1993;

84   Warczok and Utigard, 1998). The reduction process could not be solely controlled by

85   Boudouard reaction (redox reaction of a chemical equilibrium mixture of carbon monoxide

86   and carbon dioxide) (Warczok and Utigard, 1998) or chemical reaction of hydrogen with

87   fayalite combining with permeation of H_2 through silica (Massieon et al., 1992; Massieon

88   et al., 1993) since various reducing solid or gas media gave similar values. Addition of

89   magnesium seems to hinder reduction process and gave ΔH of 205 kJ/mol for Fa_{93}

90   (Massieon et al., 1993). There is one exception when fayalite was reduced at 973-1123 K

91   and 1673-1823 K using H_2 or $CO\text{-}CO_2$. The interfacial chemical reaction was put forward

92   as its reduction rate in early period agreed with McKewan's equation and a smaller ΔH

93   value of 188 kJ/mol was determined (Minowa et al., 1968). For San Carlos olivine Fo_{92}, a

94   high ΔH of 256 kJ/mol, similar to that of fayalite, was obtained at 1 atm, 1473-1773 K

95   using H_2/CO gas mixture (Massieon et al., 1993). And the addition of iron appeared to

96   decrease ΔH to 227 kJ/mol for Miyake olivine (Fo_{83}) compared with San Carlos olivine

97   (Fo_{92}) (Nagahara, 1986).

98
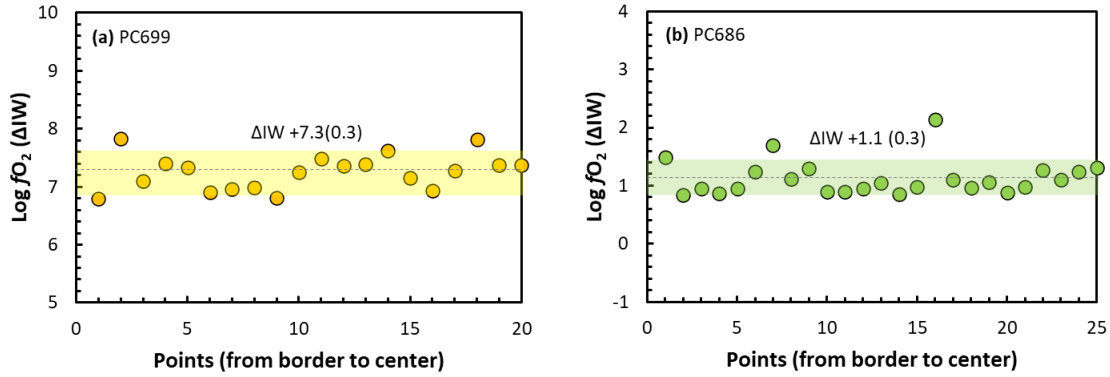
99

100 **Fig. S1.** Oxygen fugacity profile of sintered Pt-doped olivine aggregate at 1473 K. The

101 near constant oxygen fugacities across cross section of oxidized (a) and reduced (b) sample

102 indicate that new equilibrium has reached. Dashed grey line represents averaged oxygen

103 fugacity. Yellow and green filled region represent calculated standard deviation of

104 measured data points.

105

106

107

108

109
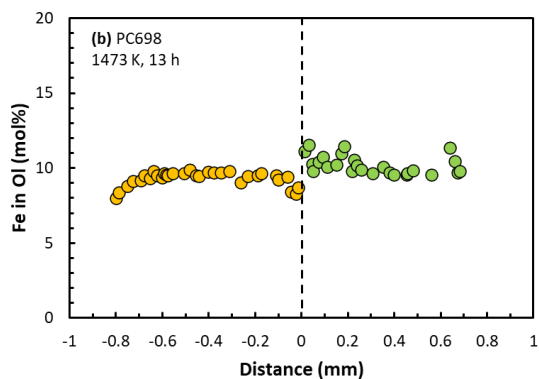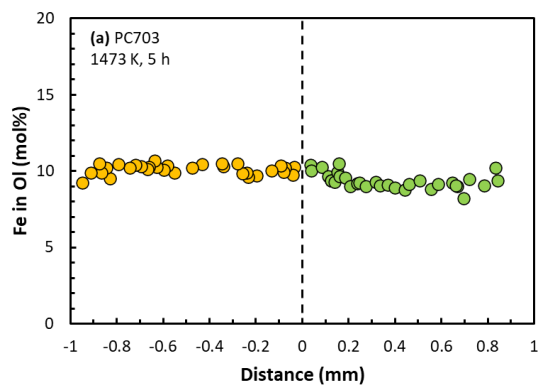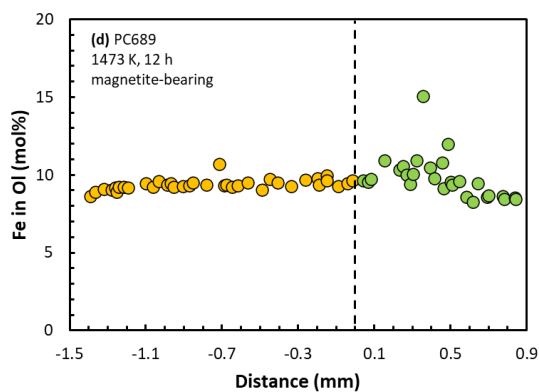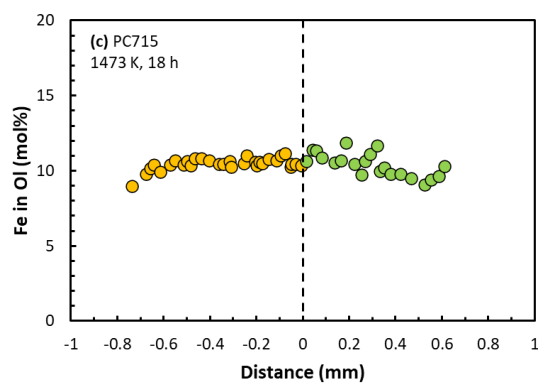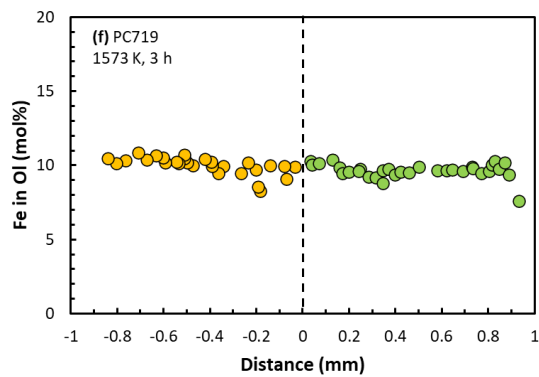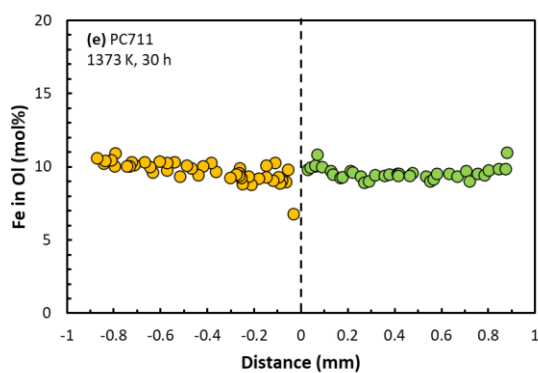
Fig. S2. Iron content in olivine surrounding Pt alloy. Yellow and green solid circles indicate

iron mole fraction in olivine in oxidized and reduced part in diffusion couple respectively.

Except several points showing large deviation, all others show well constrained iron

content with Mg# ranging from 88 to 92.

114

115

116
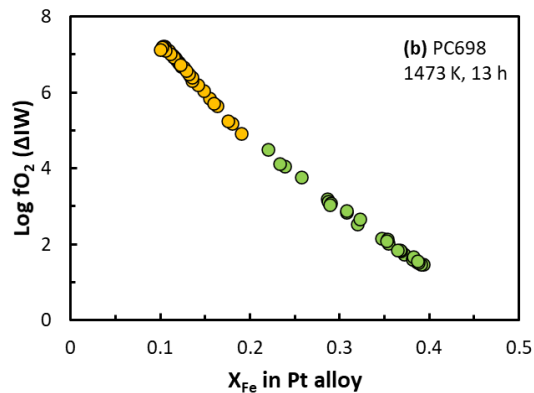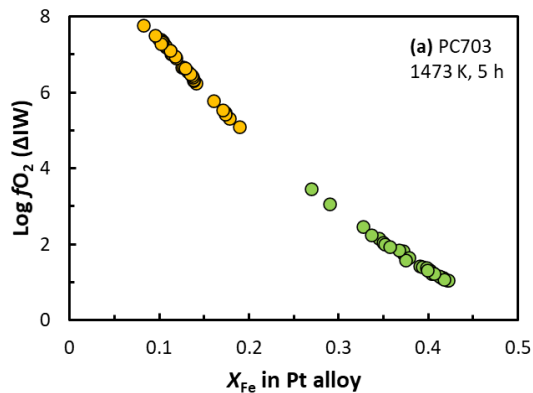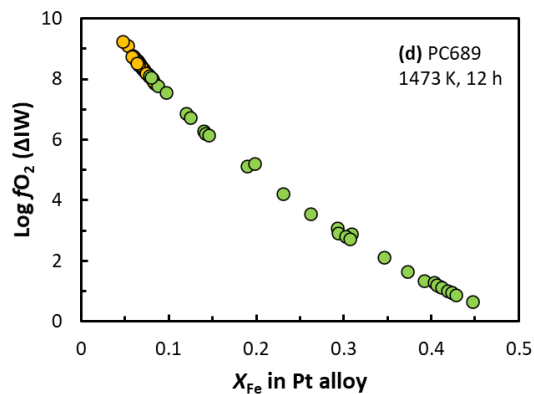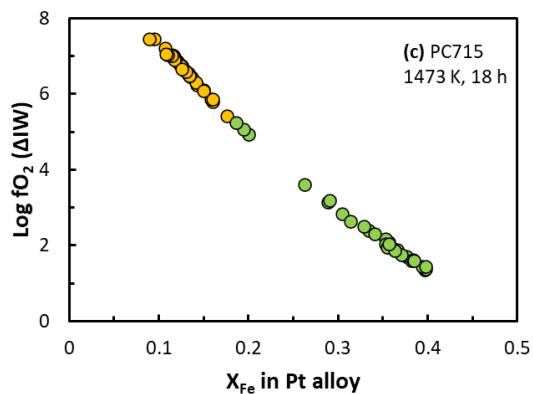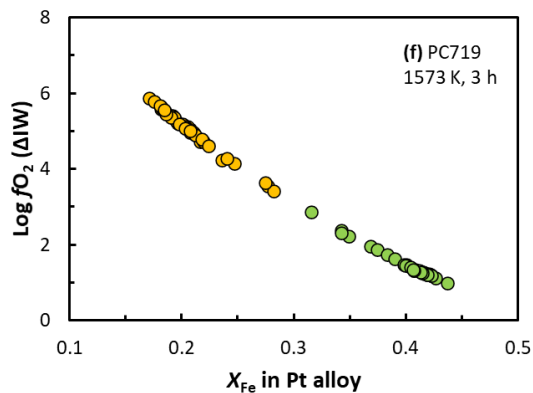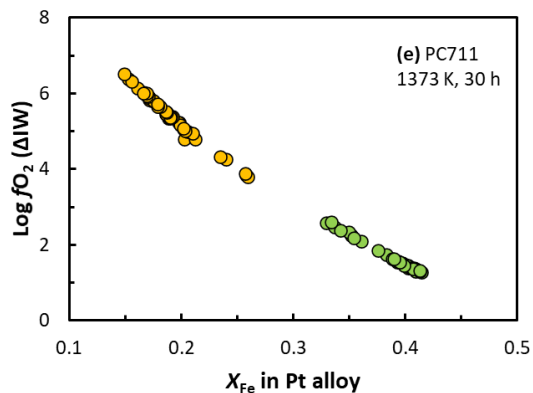
Fig. S3. Linear relationship between oxygen fugacity and iron content in Pt alloy. Yellow

and green solid circles indicate oxygen fugacities in oxidized and reduced part in diffusion

couple.

120

121

122
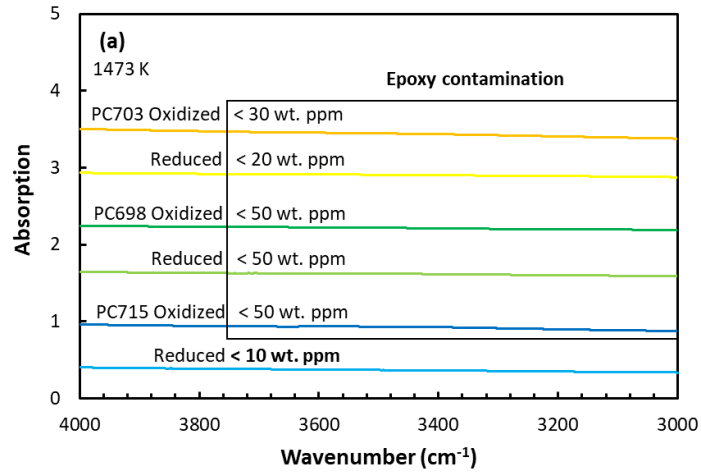
123
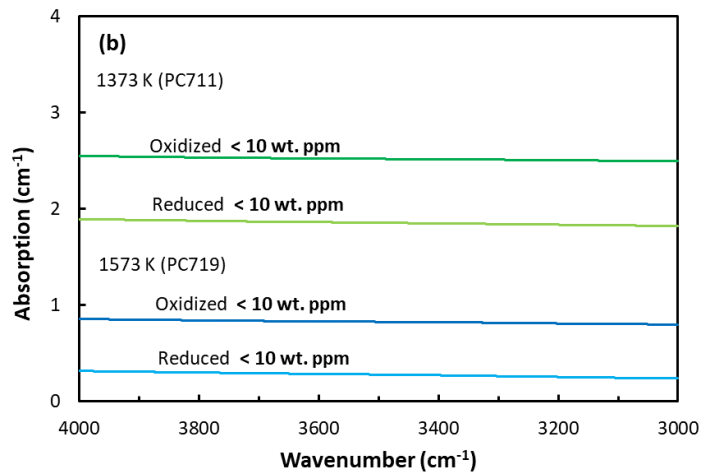
124

125   **Fig. S4.** Water contents of samples after diffusion annealing

126
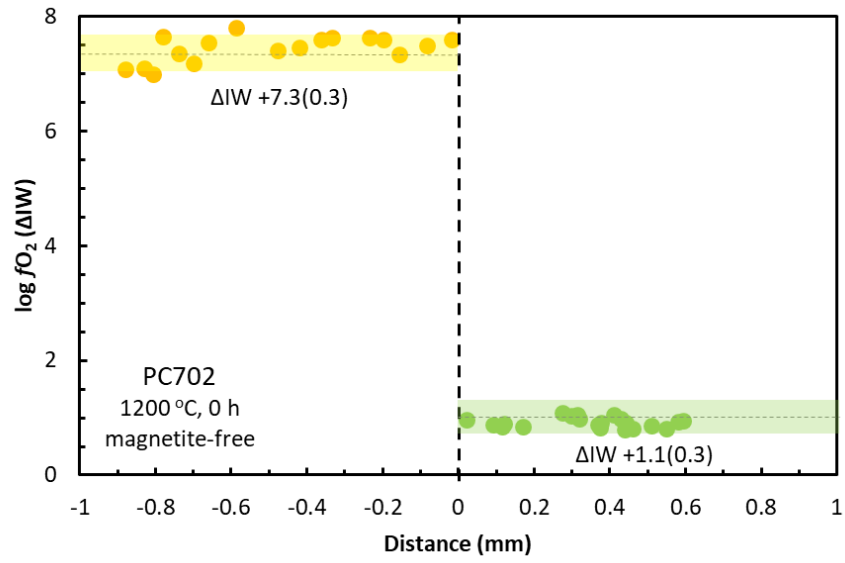
127

128   **Fig. S5.** Profile of zero-time run at 1473 K. No diffusion profile is observed.

129

130
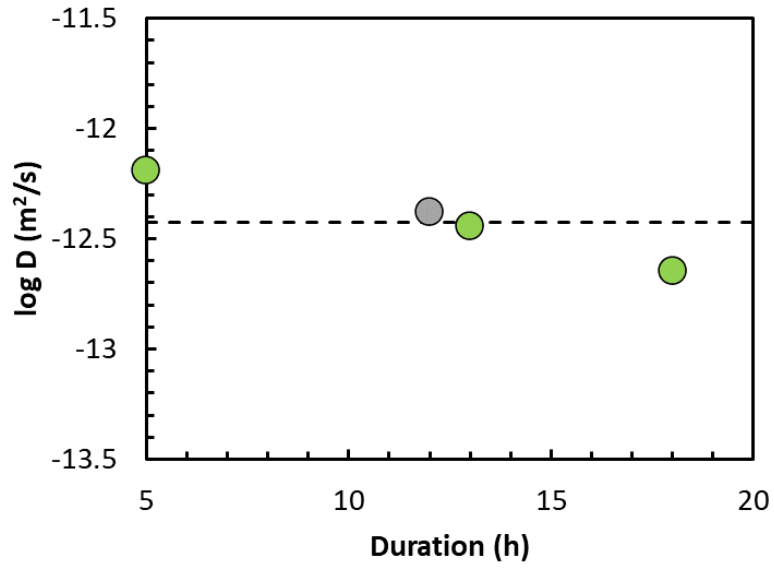
Fig. S6. Diffusion coefficient at 1473 K, 1 GPa with different durations. Green filled circles

are diffusivities from magnetite-free diffusion couples. Grey one is from magnetite-bearing

couple.

134

135

136

137
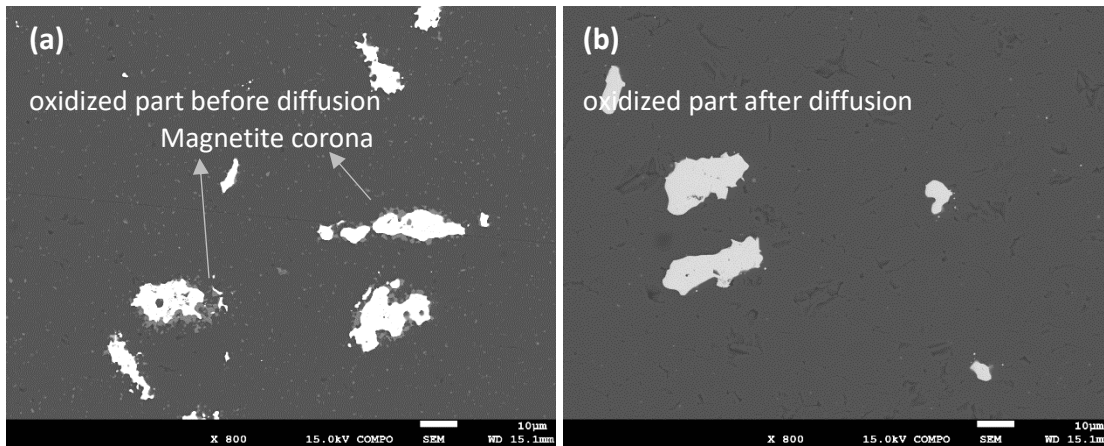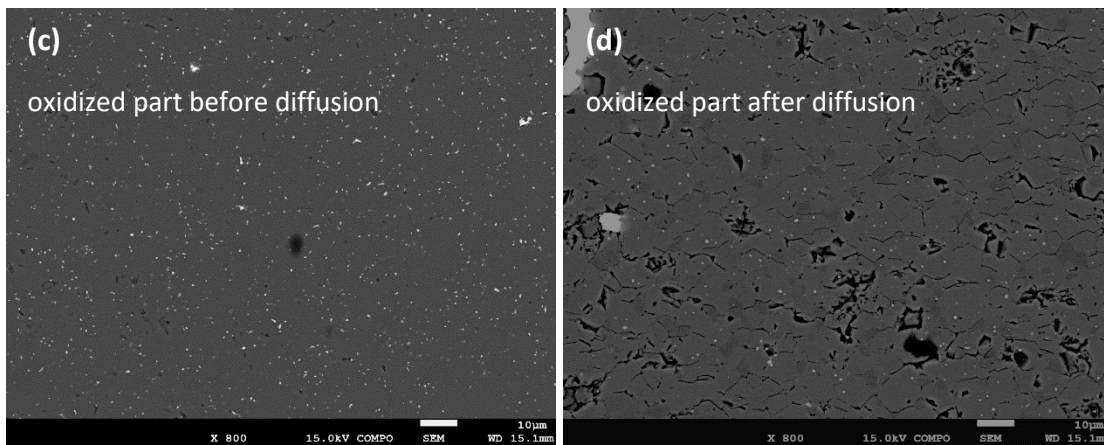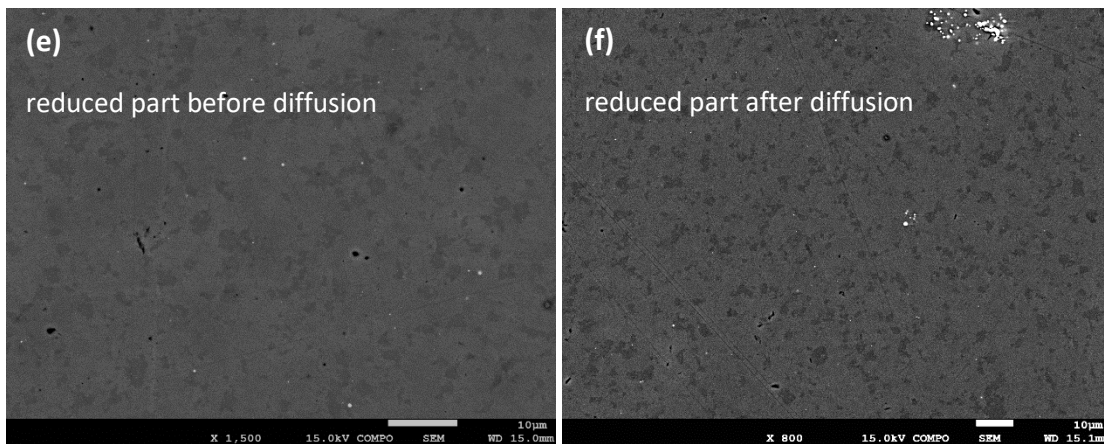
Fig. S7. Typical texture of magnetite-bearing diffusion couple before and after diffusion

annealing at 1473 K. Left column is texture before diffusion while right is texture after

diffusion.

141 **References**

142 Gaballah, I., Jeannot, F., Gleitzer, C., Dufour, L. C., (1975), Cinétique de réduction de

143 l'orthosilicate de fer Fe_2SiO_4 (fayalite) par H_2, CO et les mélanges CO+H_2. *Mém. Sci.*

144 *Rev. Métallurg.* 1975.

145 Khisina, N. R., Khramov, D. A., Kleschev, A. A., Langer, K., (1998), Laihunitization as a

146 mechanism of olivine oxidation. *European Journal of Mineralogy*. 10, 229-238.

147 Khisina, N. R., Khramov, D. A., Kolosov, M. V., Kleschev, A. A., Taylor, L. A., (1995),

148 Formation of ferriolivine and magnesioferrite from Mg-Fe olivine reactions and kinetics

149 of oxidation. *Physics and Chemistry of Minerals*. 22, 241-250.

150 Mackwell, S. J., (1992). Oxidation kinetics of fayalite (Fe_2SiO_4). *Physics and Chemistry*

151 *of Minerals*. 19, 220-228.

152 Massieon, C., Cutler, A., Shadman, F., (1992). Reduction of iron-bearing lunar minerals

153 for the production of oxygen. Univrsity of Arizona (M.S thesis), 106.

154 Massieon, C. C., Cutler, A. H., Shadman, F., (1993). Hydrogen reduction of iron-bearing

155 silicates. *Industrial & Engineering Chemistry Research*. 32, 1239-1244.

156 Minowa, S., Yamada, M., Torii, Y., (1968). A study on the formation and reduction of

157 fayalite (Fe_2SiO_4). *Tetsu to Hagane*. 54, 1203-12016.

158 Nagahara, H., (1986). Reduction kinetics of olivine and oxygen fugacity environment

159 during chondrule formation. *Lunar and Planetary Science*, 595-596.

160 Warczok, A., Utigard, T. A., (1998). Fayalite Slag Reduction by Solid Graphite.

161 *Canadian Metallurgical Quarterly*. 37, 27-39.

162   Woodland, A.B., O'Neill, H.S.C., 1997. Thermodynamic data for Fe-bearing phases

163   obtained using noble metal alloys as redox sensors. Geochim. Cosmochim. Acta 61,

164   4359-4366.

165   Wu, T., Kohlstedt, D.L., 1988. Rutherford backscattering spectroscopy study of the

166   kinetics of oxidation of $(Mg, Fe)_2SiO_4$. J. Am. Ceram. Soc. 71, 540-545.

167

168